Available online at www.sciencedirect.com

ScienceDirect

Solid Earth Sciences 8 (2023) 123–145

www.elsevier.com/locate/SESCI

Genesis and exhumation of the Kongur-Muztaghata and Maeryang gneiss domes in NE Pamir since the Mesozoic

Zhiqin Xu [a,*], Bihai Zheng [a], Shaocheng Ji [c,**], Zhihui Cai [b], Hui Cao [b], Guangwei Li [a], Xijie Chen [d], Hua Xiang [b], Fenghua Liang [b]

[a] State Key Laboratory for Mineral Deposits Research, Institute of Continental Geodynamics, Department of Earth Sciences, Nanjing University, Nanjing 210093, China

[b] Institute of Geology, Chinese Academy of Geological Sciences, Beijing 100037, China

[c] Département des Génies Civil, Géologique et des Mines, École Polytechnique de Montréal, Montréal, Québec, H3C 3A7, Canada

[d] Development and Research Center of China Geological Survey, Beijing 100037, China

Received 11 January 2023; revised 11 April 2023; accepted 11 April 2023
Available online 2 June 2023

Abstract

The Kongur-Muztaghata-Maeryang terrane in NE Pamir is considered to be the western extension of the Songpan-Ganze terrane located in the northern Tibetan Plateau. The Kongur-Muztaghata gneiss dome (KMGD) is situated in the north while the Maeryang gneiss dome (MYGD) is in the south. The KMGD comprises Triassic granites and granitic gneiss in the core and Early Paleozoic-Triassic sediments in the mantle that underwent Barrovian-type and Buchan-type metamorphisms. Based on geochemical and geochronological data, the Kongur-Muztaghata magmatic arc was formed around ~252–204 Ma due to northward subduction of the Paleo-Tethys Jinsha oceanic slab. The collision of the Kongur-Muztaghata magmatic arc and the Qiangtang terrane occurred subsequently. Previous research suggested that the KMGD was formed in the Miocene (21–8 Ma). However, our new in-situ monazite U–Pb data for the mantled metasediment shows that the KMGD was initially formed at ~198 Ma.

The MYGD is comprised of an Early Paleozoic-Triassic metasediment mantle and a Cambrian anatexis complex core that underwent Barrovian-Buchan metamorphisms. Our new structural, geochemical, and geochronological data suggest that the protolith of the Maeryang orthogneiss was formed around ~519-513 Ma, with the surrounding Early Paleozoic metavolcanic rocks erupted at ~519-508 Ma. Together, they formed the Early Cambrian magmatic complex. In-situ U–Pb dating of monazites and zircon metamorphic rims for the Triassic metamorphic rocks in the mantle indicate that the Barrovian-Buchan metamorphism in the MYGD occurred around ~206-187 Ma, likely caused by anatexis in the deep crust of the gneiss dome core. Thus, we propose that the KMGD and MYGD underwent a two-stage exhumation: the initial uplift during the Late Triassic-Early Jurassic thermo-tectonic event associated with the Cimmerian orogeny and the late rapid exhumation since the Miocene driven by the collision between the Eurasian and Indian plates.

Keywords: NE Pamir; Kongur-Muztaghata gneiss dome; Maeryang gneiss dome; Barrovian-Buchanan metamorphism; In situ monazite U–Pb dating; Late triassic-early jurassic thermo-tectonic event

1. Introduction

A gneiss dome is an important tectonic structure in orogenic systems that results from the ascent of low-density, low-viscosity, and partially molten materials from the deep crust (Eskola, 1948; Teyssier and Whitney, 2002; Yin, 2004; Whitney et al., 2004). Previous studies suggested that gneiss domes in the Pamir recorded exhumation and uplift from depths of ~30–40 km and reached their peak metamorphic conditions in the Miocene (Hubbard et al., 1997; Robinson et al., 2004, 2007, 2012; Schmidt et al., 2011, Fig. 1).

The Kongur-Muztaghata gneiss dome (KMGD) in the NE Pamir is a prominent feature, with peaks exceeding 7500 m in

* Corresponding author.
** Corresponding author.
E-mail addresses: xzq@nju.edu.cn (Z. Xu), sji@polymtl.ca (S. Ji).
Peer review under responsibility of Guangzhou Institute of Geochemistry.

https://doi.org/10.1016/j.sesci.2023.04.001

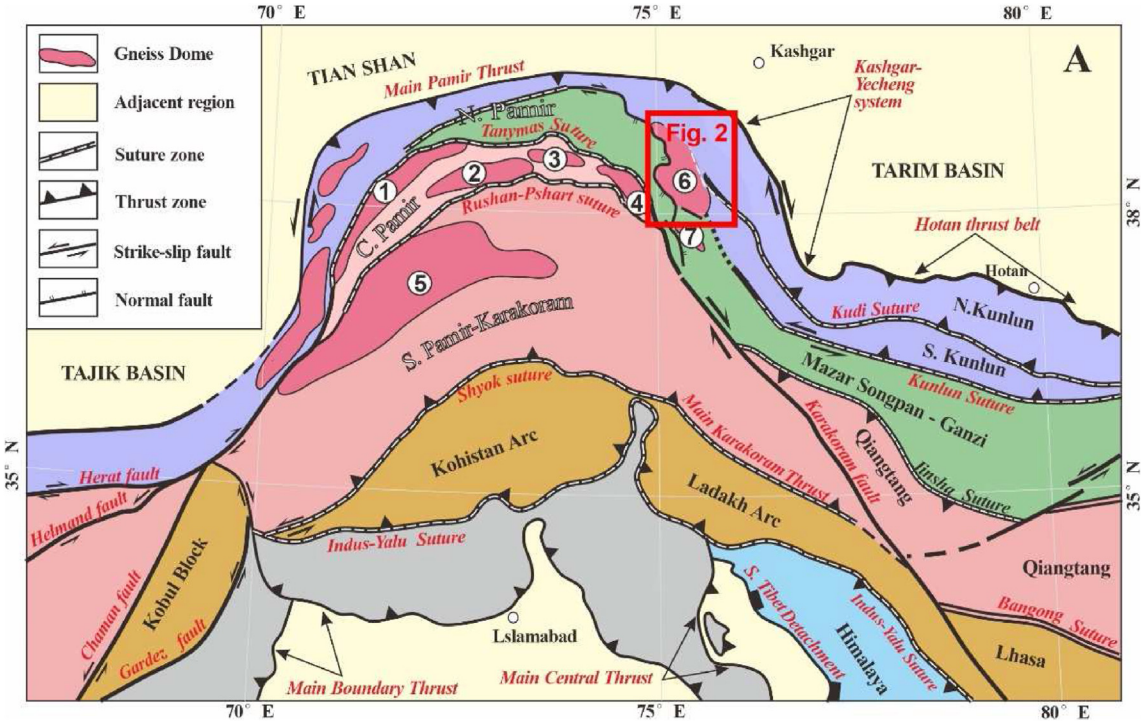

Fig. 1. Simplified tectonic map of the Pamir Salient at the western end of the Himalayan-Tibetan orogen (modified after Robinson et al., 2015). Locations of major suture zones, tectonic terranes and faults are compiled from Tapponnier et al. (1981), Burtman and Molnar (1993), Yin et al. (2002), Robinson et al. (2004) and Schmidt et al., 2011. ① Yazgulom dome, ② Sares dome, ③ Muskol dome, ④ Shatput dome, ⑤ Shakdara dome, ⑥ Kongur-Muztaghata dome, ⑦ Maeryang dome. N.PMR, North Pamir; C.PMR, Central Pamir; S.PMR, Southern Pamir; MPT, Main Pamir thrust; SS, Shyok suture; IYS-Indus, Yaluzanbu Suture; JS, Jinsha Suture; KS, Kunlun Suture.

elevation. It is composed of Late Triassic granitic plutons and surrounding high-grade metamorphic rocks. Previous studies suggested that the formation of the KMGD was partly accommodated by a south-north striking, west-dipping detachment at 21–8 Ma (Robinson et al., 2004, 2007, 2010; Cai et al., 2017), and the exhumation process continued until the present day (e.g., Sobel et al., 2011; Thiede et al., 2013). However, the initial exhumation and the pre-Cenozoic deformation history of the KMGD remain uncertain, which hinders the estimation of exhumation rates and climate impacts of the northern Pamir Salient during the Indo-Asian collision.

This study aims to investigate the pre-Cenozoic history of the Kongur-Muztaghata and Maeryang gneiss domes in NE Pamir. The authors conducted field observations and measurements to outline the structural and kinematic history of these gneiss domes. They also provided new data on their magmatic and deformation fabrics, whole-rock and in-situ geochemistry, zircon and in-situ monazite U–Th–Pb ages, mica ^{40}Ar-^{39}Ar ages, and zircon Lu–Hf isotopes to discuss the P-T-t history of high-grade metamorphism, as well as the relationship among magmatism, metamorphism, and deformation. The findings demonstrate that the Kongur-Muztaghata and Maeryang gneiss domes were formed from the hot, weak middle-lower crust of a Paleo-Tethys magmatic arc produced by the northward subduction of the Paleo-Tethys Jinsha oceanic slab. The authors proposed a multi-stage evolution model for the gneiss domes during the Late Triassic-Early Jurassic and the Miocene periods.

2. Geological setting

2.1. Pamir Salient at the western end of the Himalayan-Tibetan Plateau

The Pamir Salient is known as one of the most active tectonic regions in Central Asia, having undergone significant northward indentation of approximately 300 km (Burtman, 2010; Burtman and Molnar, 1993; Coutand et al., 2002; Cowgill, 2010) and crustal shortening of 600–900 km during the Cenozoic period (Schmidt et al., 2011; Hacker et al., 2017). This area, located at the western end of the Himalayan-Tibetan orogen, is made up of a series of northward arcuate-shaped terranes, which were formed by successive north-south collision and accretion events during the late Paleozoic and Mesozoic (Sengör and Hsü, 1984; Debon et al., 1986; Sengör et al., 1993; Yin and Harrison, 2000) as well as the Cenozoic collision between the Indian and Asian plates (Burtman and Molnar, 1993; Hubbard et al., 1997; Ratschbacher et al., 1997; Hacker et al., 2017).

The terranes in the Pamir include the Paleozoic Kunlun and Permian–Triassic Karakul-Mazar terranes (commonly grouped together as the North Pamir), the central and southern Pamir, and the Karakoram terrane, from north to south. The Main Pamir Thrust (MPT), the west Kunlun suture zone, the Jinsha suture zone, the Rushan-Pshart suture zone, and the Shyok suture zone are the boundaries for the Pamir terranes from north to south (Robinson et al., 2012; Rutte et al., 2017a; Rutte

et al., 2017b). The Paleozoic Kunlun terrane is situated in the north, bounded by the Main Pamir Thrust (MPT), and the Karakul-Mazar terrane in the south, which is considered correlative with the Songpan Ganze terrane of Tibet (Xiao et al., 2002a; Schwab et al., 2004; Robinson et al., 2012; Imrecke et al., 2019). The Kunlun terrane is bounded in the south by the north-dipping Tanymas-Torbashi thrust (or suture), considered correlative with the Jinshajiang suture of Tibet (Imrecke et al., 2019), and is considered the boundary between Asian affinity terranes in the north and Gondwanan affinity terranes in the south of the Pamir region.

The Central Pamir terrane is composed of Paleozoic–Jurassic platform rocks that are correlated with the Qiangtang terrane in Tibet (Lacassin et al., 2004; Schwab et al., 2004; Valli et al., 2008; Imrecke et al., 2019). The Southern Pamir consists of Proterozoic gneisses and Paleozoic–Mesozoic metasedimentary rocks that are equivalent to the Lhasa terrane in Tibet (Tapponnier et al., 1981; Burtman and Molnar, 1993; Brunel et al., 1994; Rumelhart et al., 1999; Schneider et al., 1999; Yin et al., 2002; Robinson et al., 2004, 2007; Schmidt et al., 2011). The Kohistan-Ladake terrane, which is bounded by the Shyok suture to the north and the Indus-Yarlu suture zone to the south (Fig. 1), consists of Cretaceous–Paleogene granitoids that are equivalent to the Gangdese batholiths in the Lhasa terrane (Burtman and Molnar, 1993; Schwab et al., 2004; Bouilhol et al., 2013). Cao et al. (2015) suggested that most of the northwest Tibetan Plateau was above sea level during the Jurassic-Cretaceous, as marine deposition was missing in the Karakul-Mazar, Songpan-Ganzi, and west Kunlun terranes during this period (Fig. 1).

2.2. Gneiss domes in Pamir Salient

In the Pamir Salient, which has been a convergent setting since the Mesozoic to Cenozoic era, several large gneiss domes made up of granitic core and high-grade metamorphic mantle are exposed. These gneiss domes account for approximately 30% of the surface exposure of the Pamir region, with typical examples being the Kurgovat and Kongur-Muztaghata gneiss domes in the Northern Pamir, the Yazgulom, Sares, Muskol and Shatput gneiss domes in the Central Pamir, and the Shakhdara gneiss dome in the Southern Pamir, as shown in Fig. 1a (Stübner et al., 2013; Rutte et al., 2017a; Rutte et al., 2017b).

The high-grade metamorphic rocks in the gneiss domes across the Pamir consist mainly of Barrovian series metapelites with peak metamorphic assemblages equilibrated at different temperatures and pressures in the Northern Pamir (e.g., the Kurgovat dome), Central Pamir, and Southern Pamir (e.g., the Shakhdara gneiss dome) (Robinson et al., 2004, Robinson et al., 2012; Schmidt et al., 2011; Hacker et al., 2017). The pressure and temperature gradually increase with successive occurrence of chlorite, biotite, garnet, staurolite, kyanite, and sillimanite, as is typical in the Barrovian series, due to crustal thickening in an orogenic belt. Previous studies have suggested that the metamorphic rocks exposed in the Central and Southern Pamir terranes were exhumed from the deep crust at depths of 30–40 km during the Oligocene-Miocene period, based mainly on U–Pb zircon, U–Th–Pb monazite, U–Pb titanite, and mica ^{40}Ar-^{39}Ar ages (Cai et al., 2017; Rutte et al., 2017a; Rutte et al., 2017b; Hacker et al., 2017; Imrecke et al., 2019).

2.3. Gneiss dome in the NE Pamir

The Kongur-Muztaghata gneiss dome (KMGD) is a large-scale structure located in the NE Pamir region, consisting of a Late Triassic granite and granodioritic pluton core, and a medium-to-high grade Barrovian series metamorphic mantle composed of the Paleozoic-Triassic series (Schwab et al., 2004; Burtman and Molnar, 1993; Robinson et al., 2009; Robinson et al., 2012; Imrecke et al., 2019). Zircon U–Pb dating of granitic gneiss from the KMGD revealed Triassic granitic protolith ages (~225–254 Ma) at the northern and western margins of the Kongur-Muztaghata pluton (Robinson et al., 2012; Imrecke et al., 2019). The neodymium isotopic compositions [εNd(O) values] obtained by Robinson et al. (2012) suggest that the granitic protolith was part of the Permian–Triassic Karakul-Mazar arc–accretionary complex. Detrital zircon U–Pb dating from the metasediments along the western margin of the KMGD provided Triassic maximum depositional ages with an age distribution similar to that of the Songpan-Ganzi terrane (Robinson et al., 2012). The schist, which lies structurally above the Triassic granitic core, displays early Paleozoic maximum depositional ages (~518-459 Ma) on the western side of the KMGD. The schist has a detrital age distribution similar to that of the Qiangtang terrane (Central Pamir, Robinson et al., 2012; Imrecke et al., 2019; Yang et al., 2010, Figs. 1 and 2).

Metamorphic rocks of Barrovian type, consisting of sillimanite-andalusite-staurolite-garnet-biotite-chlorite assemblages, are exposed in the Triassic rocks near the west normal fault of the Kongur pluton in the Muji area (Robinson et al., 2004, 2012). Kyanite and sillimanite have also been observed in early Paleozoic metamorphic rocks on the west and east sides of the Muztaghata pluton (Cai et al., 2017; see Fig. 2). The high-grade metamorphic rocks have recorded Mesozoic–Cenozoic tectonic events, with schist dated to T3-J1 from monazite inclusions in garnet. Zircon U–Pb dating results from mantling Sil-Ky bearing schist located in the western and southwestern parts of the KMGD suggest a Jurassic metamorphic event, with ages of approximately 190-170 Ma (Robinson et al., 2012) and 186.7–200.5 Ma (Zhang et al., 2018).

2.4. Cenozoic deformation in the northern Pamir

The Cenozoic deformation in the region was mainly due to the northward transpression along the Main Pamir Thrust (MPT) in the north, the right-lateral strike-slip motion along the Karakorum fault in the south, and the extension along the West Muztaghata Detachment (WMD), West Kongur-Muztaghata Fault (WKMF), Shenti Fault (STF) in the west and southwest, and the Ghez steeply east-dipping normal fault (GF) in

the east (Arnaud et al., 1993; Brunel et al., 1994; Strecker et al., 1995; Robinson et al., 2004, 2007; Amidon and Hynek, 2010; Cao et al., 2013; Cai et al., 2017; Imrecke et al., 2019; see Figs. 1 and 2). It has been suggested that the MPT accommodated around 300 km of southward intracontinental subduction of the Tarim block crust during the Cenozoic (Burtman and Molnar, 1993; Thomas et al., 1994). The initiation of the MPT is reported to have occurred in the Late Oligocene (Thomas et al., 1994; Sobel and Dumitru, 1997) or the Middle Eocene (Yin et al., 2002). The West Muztaghata Detachment was active during the Miocene east-west extension, according to Robinson et al. (2004, 2007, 2010), Cai et al. (2017), and Imrecke et al. (2019). The authors also suggest that the STF, which dips moderately to steeply to the south, is a normal fault that formed during the Cenozoic and acted as the southwestern boundary of the KMGD.

The KMGD is bounded by the Muskol shear zone to the north, the STF to the south, and the Kuke fault (KF) to the east (Robinson et al., 2007; Sobel et al., 2011; Rutte et al., 2017b; Cai et al., 2017; Imrecke et al., 2019; see Fig. 2). The NW–SE striking STF runs almost parallel to the elongated axis of the Muztaghata pluton. The KF is a sub-vertical shear zone that runs north-south and marks the eastern boundary of the KMGD (XBGMR, 1993; Sobel et al., 2011; Robinson et al., 2012; Cai et al., 2017; Imrecke et al., 2019). Biotite ^{40}Ar-^{39}Ar ages of 12-8 Ma have been reported from the southern segment of the Ghez fault, which forms part of the KF, indicating rapid exhumation during that period (Sobel et al., 2011; Cai et al., 2017).

The metamorphic rocks in the KMGD are believed to have been exhumed from depths of 30–35 km to a biotite closure temperature (300–350 °C) around ~8 Ma (Robinson et al., 2004, 2007, 2010). U–Pb dating of zircon overgrowth rims from leucogranitic veins and Ar40-Ar39 biotite dating from high-grade mylonites collected from the north side of the STF yielded ages of ~20 Ma and 12-8 Ma, respectively. These ages were interpreted as the ages for activation of the WMD (e.g., WMSZ Cai et al., 2017). Based on the above data, previous studies have suggested that the KMGD was exhumed due to a north-south-striking system of normal faults, driven by east-west extension since the Miocene only (e.g., Robinson et al., 2004, 2007, 2010; Imrecke et al., 2019).

2.5. Songpan Ganzi terrane in the northern Tibetan Plateau

The Songpan-Ganzi terrane is located along the northern Tibetan Plateau and extends from the Mazar-Tianshuihai terrane in the NE Pamir, the Tianshuihai terrane in the western Tibetan Plateau, the Bayan Har terrane in the central, to the Songpan Ganzi terrane in the east. It is displaced by the large-scale NE–SW trending Altyn Tagn Fault in the central part.

The Songpan-Ganzi terrane was formed during the Middle to Late Triassic period when the Paleo-Tethys oceanic lithospheric slabs closed along a double-vergent subduction system. This is represented by the Kangxiwa-East Kunlun-Anyimaqen suture zone to the north and the Jinsha-Ailaoshan suture zone to the southwest (Xu et al., 1992; Roger et al., 2010; de Sigoyer et al., 2014). The formation of both accretional Triassic magmatic arcs, including the Kunlun arc of ~273-223 Ma (Jiang et al., 2013; Liu et al., 2015; Zhang et al., 2005; Zhang et al., 2016) to the north, and the Yidun arcs of ~245-215 Ma (Reid et al., 2005a; Reid et al., 2005b), were also associated with this event. The Late Triassic-Middle Jurassic orogen in the Songpan-Gangze terrane is characterized by south-verging folds and thrusts in the Paleozoic-Triassic sedimentary covers, as well as a large-scale south-directed sole decollement between the Neoproterozoic basement and the Early Paleozoic meta-sediments (Mattauer et al., 1992; Xu et al., 1992; Roger et al., 2010; de Sigoyer et al., 2014; Fig. 1).

A thick turbidite, estimated to be between 5 and 15 km in thickness and to have formed during the Middle-Late Triassic period, occurs in the Songpan-Gangze orogen, specifically in the Xikang and Bayan Har groups (e.g. Xu et al., 1992; Yin and Harrison, 2000; Weislogel, 2008). This flysch basin was triangular and located in deep marine waters (e.g. Xu et al., 1992; Yin and Harrison, 2000; Weislogel, 2008). It was likely developed from a back-arc basin created by northward subduction of the Jingsha oceanic lithospheric slab (Burchfiel et al. 1995; Hsü et al., 1995).

The Triassic turbidites in the area were infiltrated by numerous granitic plutons, primarily aged between 228 and 195 Ma (Zhang et al., 2006, 2007; Xiao et al., 2007; Yuan et al., 2010, Fig. 2). Previous researchers have suggested that most S-type granites result from crustal melting (Roger et al., 2004; de Sigoyer et al., 2014). Some gneiss domes, such as the Jiajika and Markam gneiss domes, can be found in the south-eastern part of the Songpan Ganzi terrane and are associated with Late Triassic granitic plutons (Xu et al., 2020; Zheng et al., 2020). These gneiss domes are characterized by Triassic granitic cores and Triassic metamorphic rocks that include sillimanite, staurolite, andalusite, garnet, and biotite. Many lithium pegmatites were also intruded into these rocks during the Late Triassic to Middle Jurassic period (Xu et al., 1992; Xu et al., 2016; Xu et al., 2020; Fu et al., 2017; Zhao et al., 2019; Zheng et al., 2020).

3. Field observations and structural analyses of the Kongur-Muztaghata gneiss dome (KMGD)

The Kongur-Muztaghata gneiss dome (KMGD) can be divided into two structural units from bottom to top. The lower unit comprises the Triassic Kongur-Muztaghata granitic pluton, which consists of magmatic granite and marginal granitic gneiss in the core. The upper unit is dominated by high-grade Barrovian-Bachan metamorphic rocks derived from the Early Paleozoic to Triassic sequence in the mantle (Fig. 2).

3.1. Domal structure of the Kongur-Muztaghata pluton

The Kongur-Muztaghata pluton exhibits an NNW-SSE trending ellipsoidal domal structure that stretches over ~140 km in length and reaches a maximum width of ~80 km

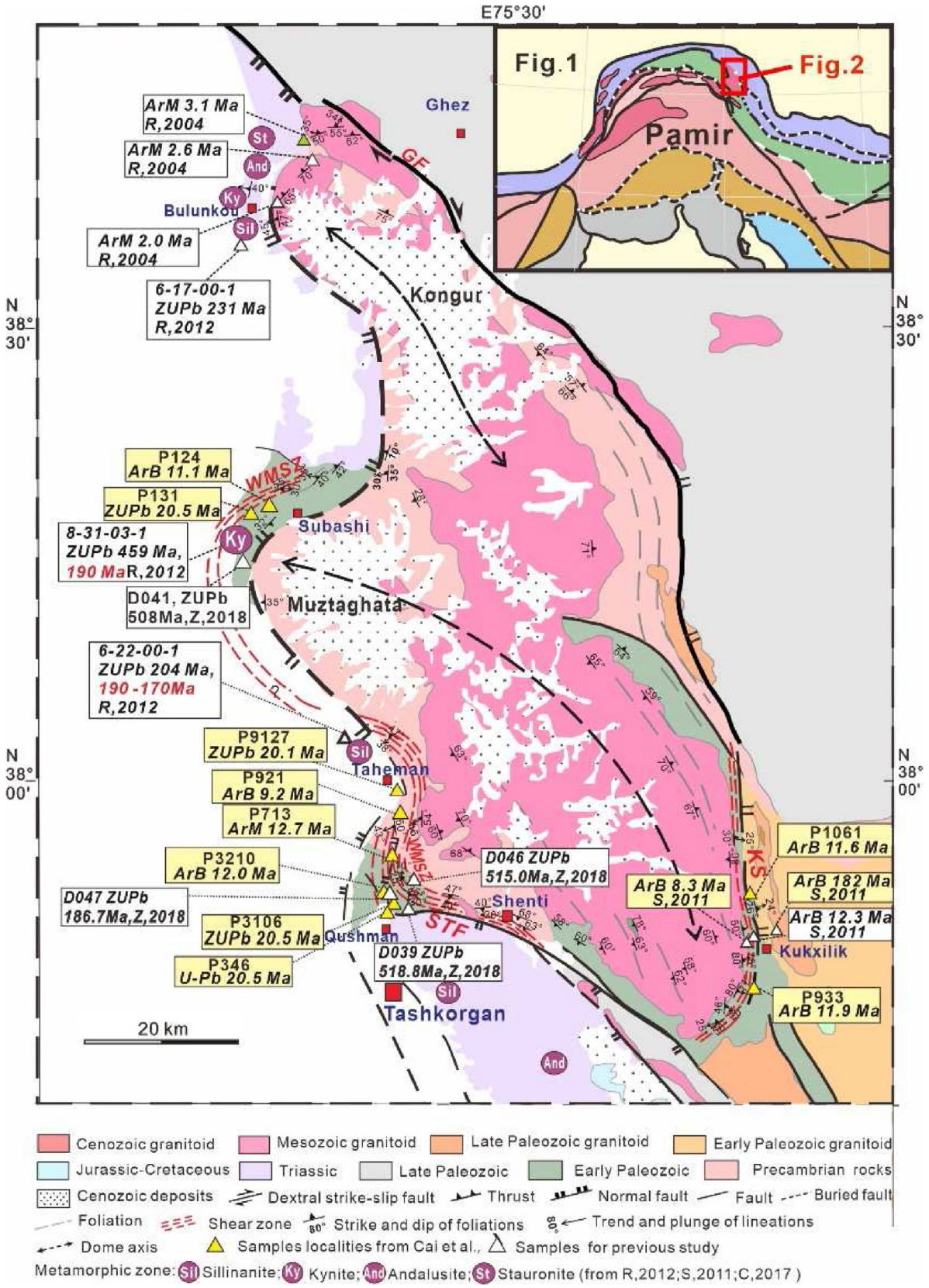

Fig. 2. Simplified tectonic map of the Kongur-Muztaghata gneiss dome (KMGD) in the NE Pamir, western end of the Himalayan-Tibetan orogen (Modified from Cai et al., 2017). Extensional faults such as Shenti fault (STF), Ghez fault (GF) and Kuke Fault (KF), crystallization ages of the Kongur-Muztaghata pluton, and protolith ages of the mantling metamorphic rocks are compiled from XBGMR, 1993; Robinson et al. (2004, 2012) (R); Zhang et al. (2018) (Z); Cai et al. (2017) (C); Schmidt et al., 2011 (S). The other age data are from this study. WKL, West Kunlun terrane; K, Kongur pluton; M, Muztaghata pluton; Tr, Triassic granite; Trgn, Triassic granitic gneiss; WMD, West Muztaghata Detachment; WMSZ, West Muztaghata shear zone; SWMD, Southwest Muztaghata Detachment.

(Fig. 2). The margin of the pluton is about ~20–24 km wide and comprises granitic gneiss, augen granitic gneisses, and amphibole-plagioclase gneisses. The outward foliation and stretching lineation are deeply dipping. In the southern part of the Muztaghata pluton, the roof between the granite and granitic gneiss is characterized by gently dipping foliations that slope at an angle of less than 30° (locations P4-3, P4-4, P4-5, P4-6, and P4-7 in Fig. 3).

A ring-shaped mylonitic zone with a thickness of ~1 km crops out between the Kongur-Muztaghata pluton and mantling Triassic and Early Paleozoic metamorphic rocks. The mylonitic zone, which is composed of the lower granitic mylonite and upper mylonitic metasediments, is characterized by outward steep-dipping radial foliations (~50–70°) and transverse stretching lineation, which showing a domal structure around the Kongur-Muztaghata pluton (Figs. 3 and 4).

The microstructures of the mylonitic zone along the eastern and southeastern flanks of the Muztaghata pluton were analyzed through samples P5-1, P9-7, and P5-2 from the lower granitic mylonite (Fig. 5a–e) and samples P10-6 and P10-7 from the upper mylonitic schist in the Paleozoic-Triassic mantling rocks (Fig. 5f–g). The results showed that the eastward steep-dipping foliations, transverse stretching lineation (La), and shear-sense indicators such as S–C structure and mica fishes indicated a southeastward normal slip shear sense (Fig. 5a–g). On the southwestern flank of the dome, the granitic mylonite (P6-1, P6-4, and P6-7 in Fig. 6a–d) and mylonitic mica-quartz schists (P4-1 and P6-4 in Fig. 6e–f) showed southwestward steep-dipping foliations with σ-type feldspar porphyroclasts, mica fishes, and S–C structures indicating a consistent southwestward down-dip slip shear sense (Fig. 6a–f).

3.2. Mantling metamorphic rocks in the KMGD

The Kongur-Muztaghata pluton is overlaid by metamorphic rocks that originated from the Early Paleozoic and Triassic sediments (XBGMR, 1993; Robinson et al., 2012; Cai et al., 2017). Our study showed that the mantling metasediments in the KMGD consist of gneisses and schists containing sillimanite, andalusite, kyanite, staurolite, garnet, and biotite. These rocks underwent intense ductile deformation, which produced continuous axial-plane foliations (S2) parallel to the western flank of the pluton, down-dip stretching lineation, and kinematic indicators of normal slip. The early foliation (S1), which was initially sub-horizontal and quasi-parallel to the roof of the Muztaghata pluton, has been deformed to develop upright, tight folds with sub-horizontal hinge lines (Fig. 5a). These results are in contrast to previous studies (XBGMR, 1993; Robinson et al., 2012; Cai et al., 2017).

4. Field observations and structural analyses of the Maeryang gneiss dome (MYGD)

The Maeryang gneiss dome (MYGD) is situated in the southern part of the KMGD and comprises three NW–SE trending Pre-Ordovician orthogneiss zones, as well as the overlying Cambrian to Triassic cover that has undergone metamorphism and deformation (Robinson et al., 2012; Zhang et al., 2018) (Figs. 2 and 7). The dominant rocks in the granitic gneiss zones are anatexis felspar-rich orthogneiss with a Cambrian emplacement age (Figs. 8 and 9, see details in Section 6), which exhibit a moderately dipping foliation to the northeast (50–60°) (Fig. 7). Despite experiencing amphibolite-facies metamorphism, the Cambrian meta-sedimentary strata have a strike of NW 300–330° and dip to the northeast at an angle of 30–50°. These strata mainly consist of garnet-bearing schist (gneiss), biotite schist, quartzite, biotite plagioclase-quartz leptynite (meta-rhyolite), amphibolite (meta-basalts), magnetite layers, and minor marble (Zhang et al., 2018). The volcanic rocks (meta-rhyolites and meta-basalts) account for approximately 30% of the sequence's thickness, while the sedimentary rocks make up approximately 70% (Zhang et al., 2018). The magnetite layers or lenses are primarily found between the amphibolite (or meta-basalt) or bimodal volcanic sequence and biotite schist or quartzite. The zircon U–Pb data from meta-rhyolite samples D050, D046, and D029 indicate that the deposition age of this amphibolite-facies sequence is Early to Middle Cambrian, approximately 508–519 Ma (Zhang et al., 2018) (Fig. 7).

Our study focuses on the northern Maeryang granitic gneiss zone and the mantle Early Paleozoic-Triassic metamorphic rocks that cover an area of approximately 50 km on the northeast flank of the Maeryang granitic gneiss zones.

4.1. Domal structure in the Maeryang gneiss dome

Many shear sense criteria, including σ- and δ-type rolling porphyroclasts of feldspar, S–C structure, garnet pressure shadows, mica fishes, and outcrop scale asymmetric folds, indicate a radial shear sense in the mantling Early-Paleozoic-Triassic rocks of the Maeryang gneiss dome. The SE part of the dome is dominated by top-to-SEE shear, the NW part by top-to-NE shear, and the N part by top-to-southwest shear (Fig. 8,-9). These observations suggest that an incomplete domal structure developed in the northeastern part of the MYGD, while the western part of the dome was covered by Quaternary sediments.

4.2. Metamorphism and anatexis in the Maeryang gneiss dome

Within the mantling rocks of MYGD, four metamorphic zones can be distinguished based on their mineral assemblages and textures: sillimanite, andalusite, garnet, and biotite metamorphic zones (Fig. 7).

To determine the pressure-temperature (P-T) conditions of metamorphism in the MYGD, conventional geothermobarometers were utilized on five samples: two from the eastern side (P11-6-1, P11-6-3) and three from the northern side [P7-1(1), P7-1(3), and P7(2)] of the mantling rocks. These samples consist mainly of metapelites with garnet, biotite, sillimanite, andalusite, plagioclase, K-feldspar, and quartz, along with minor minerals such as ilmenite, zircon, monazite, and apatite. It should be noted that needle-shaped sillimanite crystals are commonly oriented along late extensional shear

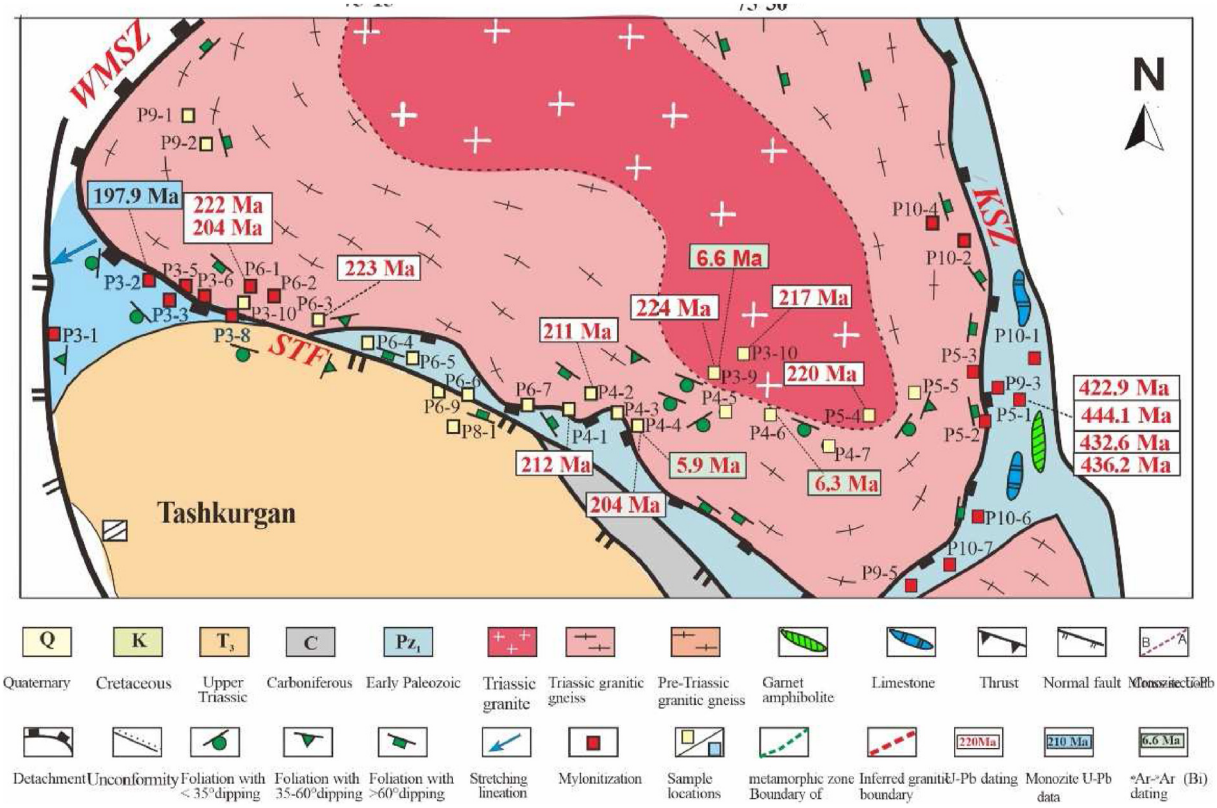

Fig. 3. Structural map of the south Muztaghata gneiss dome, showing the relationship among the domal structure and the STF system. The geochronological data are indicated. Modified from the 1:250,000 geological map of the west Kunlun (XBGMR, 1993).

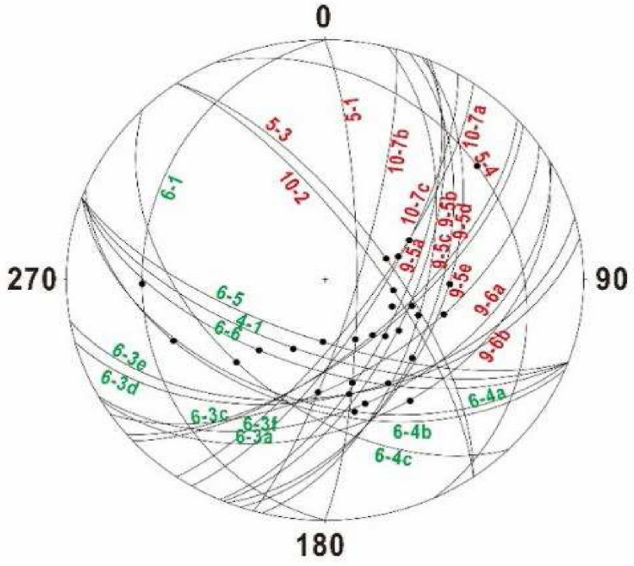

Fig. 4. Stereographic projection of the foliation and stretching lineation measured from the eastern (red) and western (green) flanks of the Muztaghata pluton.

bands that obliquely cross the main foliation in the metapelites. The garnet grains occur as subhedral porphyroblasts (0.4–5.0 mm in diameter) or fine grains in the matrix. The garnet porphyroblasts have cores of alm63-68, prp23-30, grs3-6, sps1-5 and rims of alm69-77, prp14-25, grs4-8, sps2-9 (Table S1, Fig. 9a–b). The Mg content decreases progressively from the core to the rims, whereas Mn and Ca show slight increases, and Fe increases significantly. The small garnets exhibit similar compositions to the rims of the garnet porphyroblasts.

Plagioclase, with an32-46 composition, is commonly found as a xenoblastic matrix phase in the metapelites, but can also occur as inclusions in garnet. Muscovite, preferentially aligned parallel to the foliation, has a Si content of 3.15–3.20 per formula unit (p.f.u.), TiO_2 content of 0.34–0.88 wt%, a K/(K+Na) ratio of 96, and Mg# of 56–60 (unpublished data) in samples P7-2-1 and P11-6-1. Biotite primarily occurs as a matrix phase but can also be found in shear bands or garnet pressure shadows. Inclusions of biotite in garnet are occasionally observed. The matrix biotite has a composition ranging from Mg#50 to 68 (Table S2), and zonation is not systematic. Larger biotite grains exhibit relatively lower Mg# but higher TiO_2 concentrations than smaller grains, which are found as symplectites with plagioclase.

To determine the peak P-T conditions, both the core and mantle compositions were analyzed. The data obtained from the five metapelite samples show peak temperatures ranging from 686 to 730 °C and pressures ranging from 470 to 740 MPa (Fig. 10c). To evaluate the retrograde metamorphic conditions, the rim compositions of garnets or small garnets in the matrix were determined. It was assumed that they have maintained local chemical equilibrium with adjacent symplectic biotite/muscovite and plagioclase. The data from the

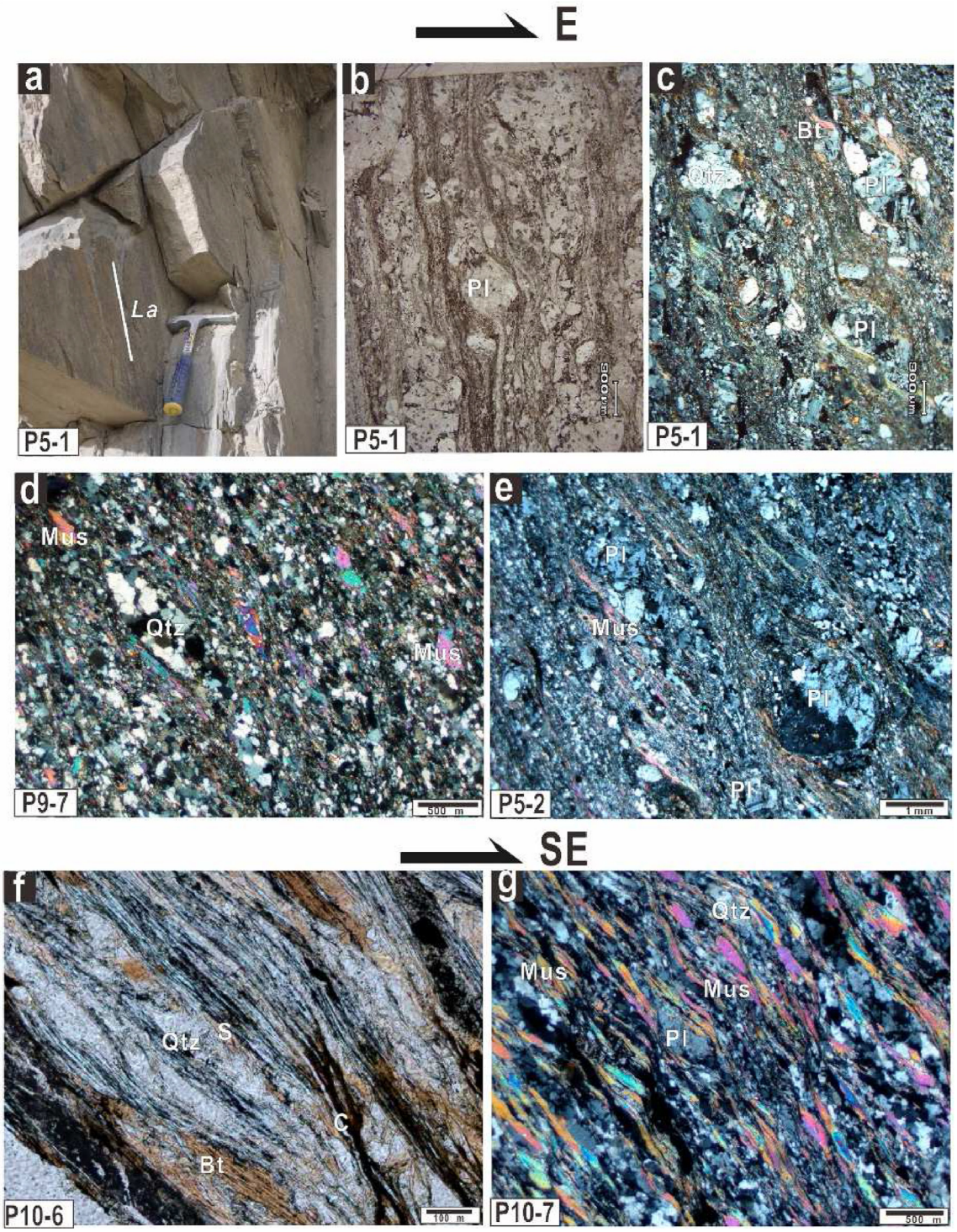

Fig. 5. Mylonitic zones along the eastern and southeastern margins of the Muztaghata pluton, which are composed of lower granitic mylonite (a–e) and upper mylonitic metasediment of Silurian schist (f–g). (a) A field photo of the mylonitic zone at the eastern margin of the Muztaghata pluton, showing the eastward steep-dipping foliation and down-dip lineation (La). (b–e) Lower granitic mylonite characterized by σ-type feldspar porphyroclasts, mica fishes and S–C structures indicating normal shear sense. (f–g) Upper mylonitic schist, characterized by S–C structure and mica fishes, indicating normal slip shear sense.

samples indicate that retrograde metamorphism took place at temperatures ranging from 555 to 631 °C and pressures ranging from 260 to 510 MPa (Fig. 10c). These results suggest that the MYGD was initiated under middle-lower crust conditions (~17–27 km deep, assuming an average rock density of 2.8 g/cm3) with geothermal gradients of 27–40 °C/km. Retrograde metamorphism occurred at depths of ~9.5–18.6 km with geothermal gradients of 34–58C/km during the exhumation of the gneiss dome.

Numerous striped, lenticular, and folded felsic veins that are parallel to the foliation are present in the Early-Paleozoic to Triassic, and high-temperature to low-pressure

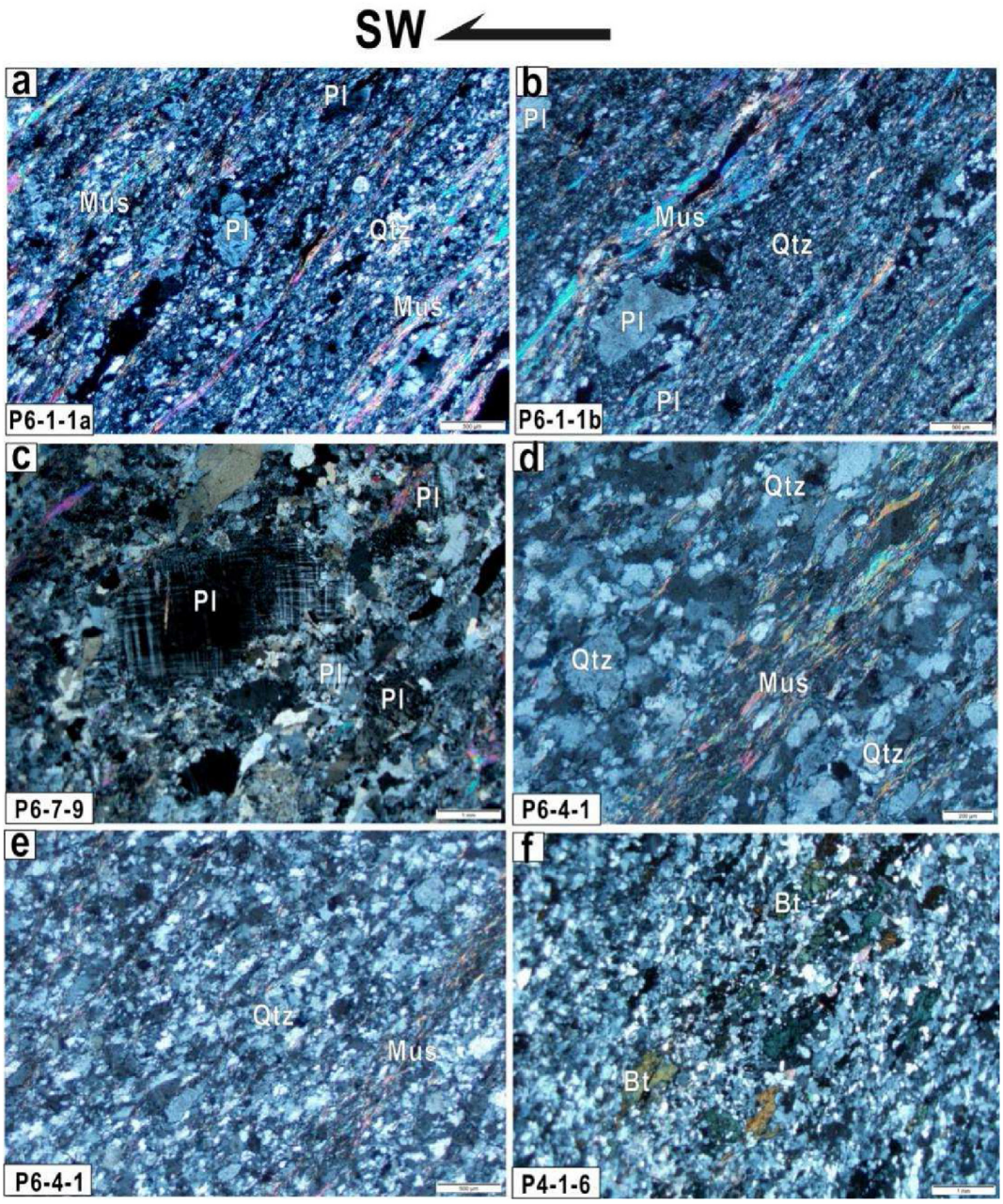

Fig. 6. Petrographic photos of mylonites from the southwestern margin of the Muztaghata pluton, which are composed of the lower granitic mylonite (a–c) and upper mylonitic metasediment of Paleozoic quartz schist (d–f). (a–c) Granitic mylonite with westward steep-dipping foliations and σ-type feldspar porphyroclasts, mica fish and S–C structures, indicating southwestward down-dip slip shear sense. (d–f) Mylonitic mica-quartz schists, characterized by S–C structures and mica fishes, indicating a southwestward normal slip shear sense. Bt-Biotite; Pl-Plagiclase; Qtz-Quartz; Mus-Muscovite.

metasedimentary rocks that mantle the Maeryang gneiss dome (Fig. 11). These veins suggest that the high-temperature to medium/low-pressure metamorphism was accompanied by anatexis from the deep crust.

5. Geochemical properties and Lu–Hf isotope data

5.1. Whole rock geochemistry of the Kongur-Muztaghata gneiss dome

Most of the analyzed intrusive rocks were found to be fresh, with a loss on ignition (LOI) of less than 0.8 wt% (Table S3). On the SiO_2 vs. K_2O diagram (Fig. 12a, Peccerillo and Taylor, 1976), the intrusive rocks have SiO_2 contents ranging from 68.35 wt% to 76.33 wt%, indicating that they belong to the high-K to medium-K calc-alkaline magma series. These rocks have ACNK values less than 1.1 and AI values (molecular (Na+K)/Al) less than 0.8 (Table S3), which suggests that they are meta-aluminous igneous rocks (Frost et al., 2001, Fig. 12b).

The rocks have a sum of rare earth elements (∑REE) contents of 57–183 ppm. The chondrite-normalized REE patterns are relatively uniform, with nearly flat heavy (H) REE segments and significant light (L) REE enrichment (LREE/HREE = 3.9–16.8). They exhibit negligible to very weak

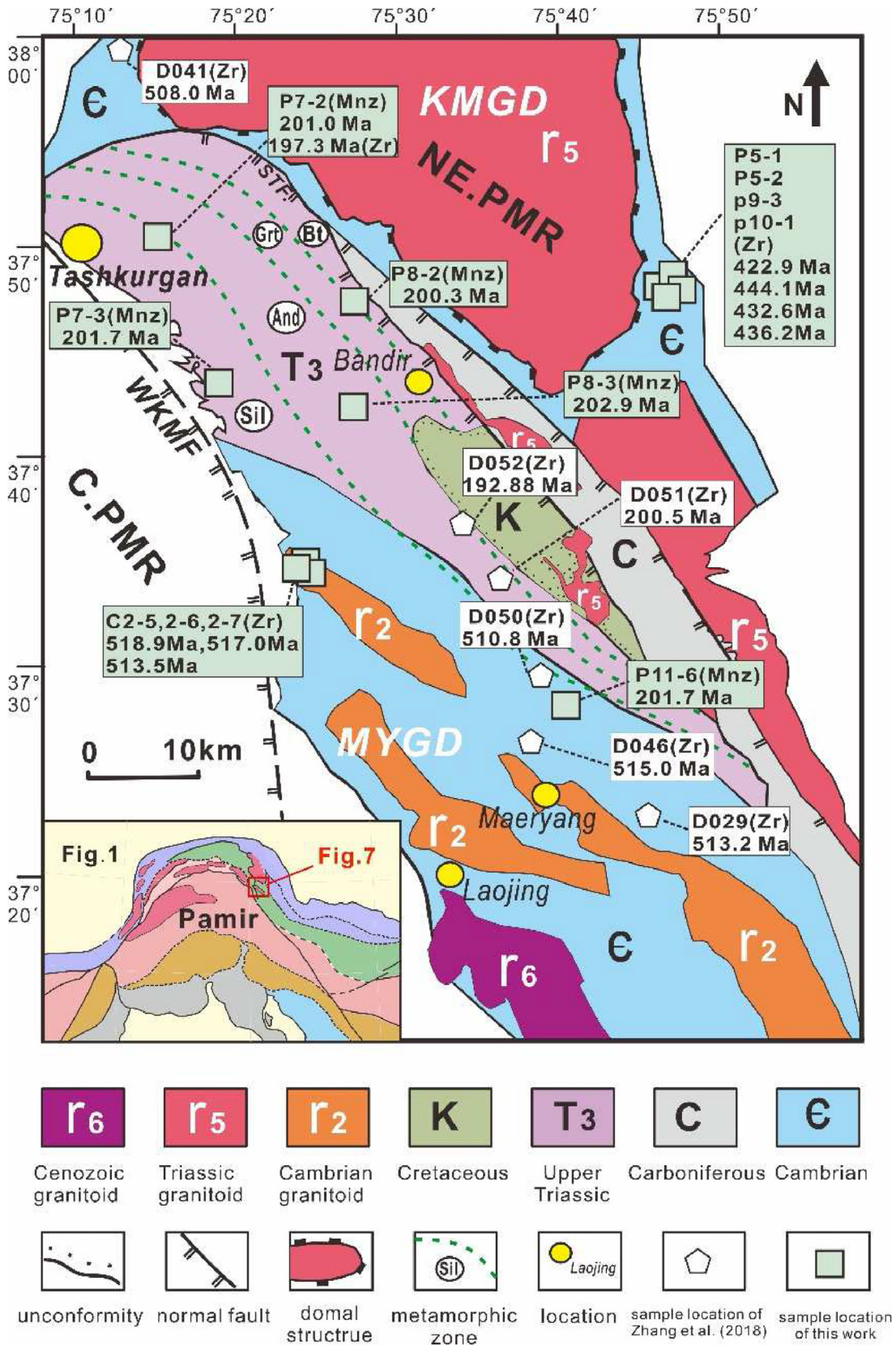

Fig. 7. The geological map of the Maeryang gneiss dome (MYGD) (modified from the geological map of XBGMR, 1993). Three NW–SE trending Cambrian migmatized granitic gneiss zones (r_2) are outlined. They are surrounded by Cambrian metavolcanic rocks and Triassic metapelitic rocks, which underwent HT-LP metamorphism during the Jurassic. From the inside out, the metamorphic zone can be divided into sillimanite, andalusite, garnet and biotite zones. Gently slipping foliation, transverse stretching lineation and shearing sense develops in the mantling metamorphic rocks, all indicate a radial outward domal structure.

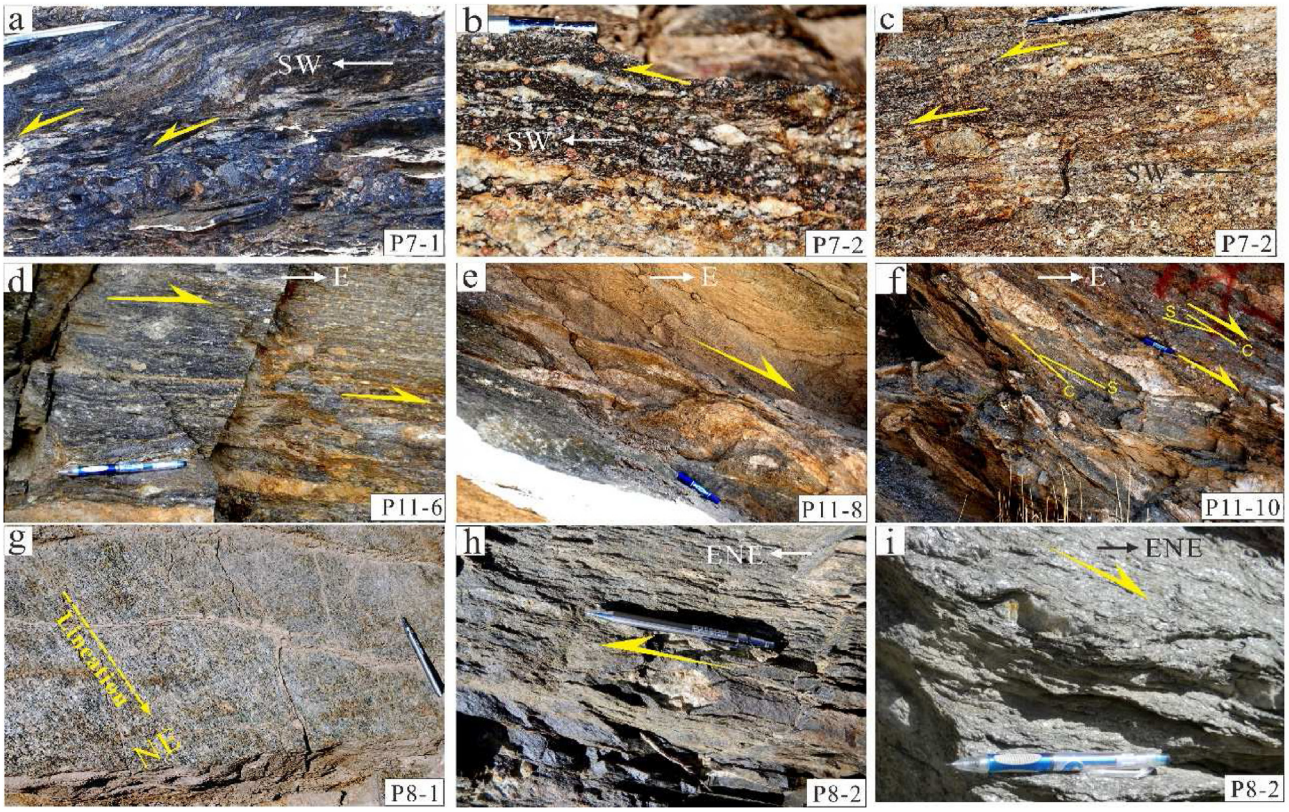

Fig. 8. Field photos from the Triassic Sil-And-Grt-Bt-bearing schist of the northeastern Maeryang granitic pluton (MYGD). Top-to-the-E, NE and ENE shearing senses are indicated by σ-type porphyroclasts of felspar (a, b, c, d, e, f, h, i), S/C structure (a, f) and stretching lineation (g).

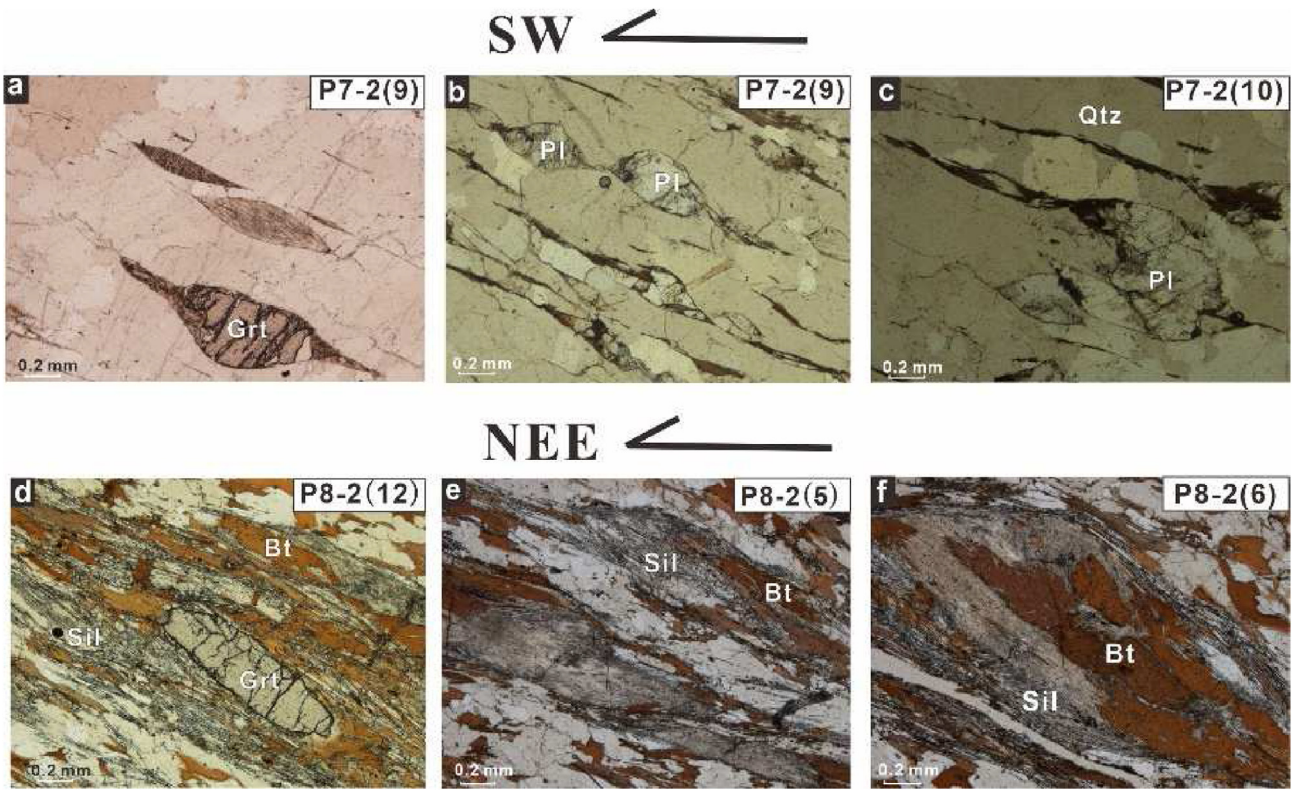

Fig. 9. Thin-section photos from the Sil-And-Grt-Bt bearing schist of the northeastern Maeryang granitic pluton (MYGD). Top-to-the-NE and NEE shearing senses are indicated by σ-type porphyroclasts of Pl and Grt (a–d), as well as asymmetric biotite fish (e–f). Bt-Biotite; Sil-Sillimanite; Pl-Plagioclase.

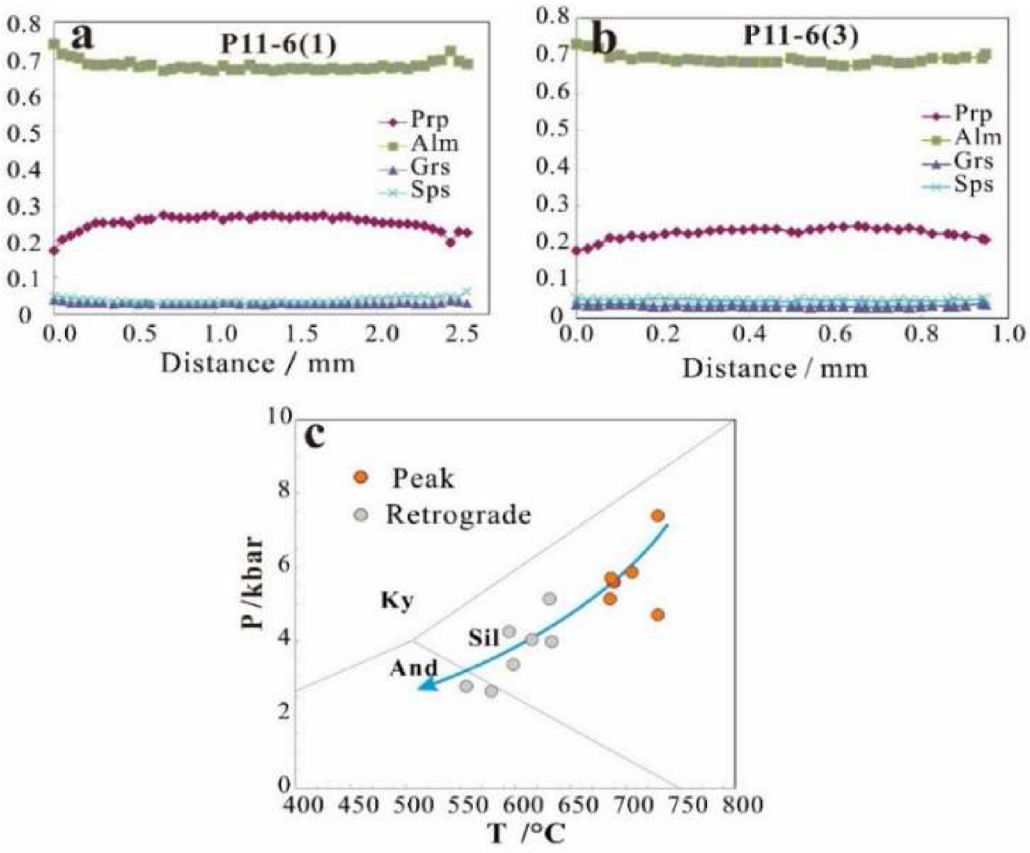

Fig. 10. (a–b) Typical compositional profiles of garnet porphyroblasts from samples P11-6(1) and P11-6(3). (c) P-T-t path inferred from the microprobe data of metapelites from the western flank of the Muztaghata pluton.

negative Eu anomalies (Eu*/Eu = 0.39–1.28) and are enriched in large ion lithophile elements (LILEs) and depleted in high field strength elements (HFSEs), with weak negative Nb and Ta anomalies, and P and Ti depletion (Fig. 13a and b). The Eu and Sr negative anomalies are possibly due to plagioclase fractionation (Green, 1994). The negative Nb and the enrichment in LILEs suggest a subduction-related component in the source area. These patterns are similar to those of average lower crustal rocks (Taylor and McLennan, 1985). In the (Zr+Nb+Ce+Y)-(Na2O+K2O/CaO) classification diagram (Fig. 12c), the granites are plotted in the unfractionated I- and S-type granite (OGT) fields. In the Yb vs. Ta, Y vs. Nb, and Y+Nb vs. Rb diagrams (Fig. 12d–f), the samples are classified as volcanic-arc granites and syn-collisional granites (Syn-COLG and VAG fields).

5.2. Zircon Lu–Hf isotope of the Kongur-Muztaghata gneiss dome

The zircon Hf isotope analyses were carried out using a Nu Plasma HR MC-ICP-MS (Nu Instruments Ltd, HK) coupled with a Geolas 2005 laser-ablation system, with a spot size of 32 μm and a repetition rate of 10 Hz, at the State Key Laboratory for Mineral Deposits Research, Nanjing University. Zircon 91500 was used as the reference standard, with a recommended 176Hf/177Hf ratio of 0.282295 ± 0.000027. A decay constant of 1.865×10^{-11} a^{-1} for 176Lu (Scherer et al., 2001) and the present-day chondritic ratios of 176Hf/177Hf = 0.282772 and 176Lu/177Hf = 0.0332 (Blichert-Toft and Albarede, 1999) were adopted to calculate the εHf(t) values. A total of 122 zircon grains from six granite samples were analyzed for the Hf isotopic composition. The results are given in Table S4. All analyzed zircon grains showed low 176Lu/177Hf ratios (<0.01), but widely variable 176Hf/177Hf ratios of 0.281206–0.282714 and corresponding εHf(t) values of −11.8-2.6 with a peak at −4–0 (Table S4, and Fig. 13c and d). The TDM2 (Hf) model ages range from 1.130 to 2.498 Ga, with a major peak at ~1.420 Ga. In addition, about 86% of the analyzed grains have negative εHf(t) values (Fig. 13d).

6. Geochronological data

To determine the chronology of thermo-metamorphic and tectonic events in the KMGD and MYGD, we collected samples from granite, granitic gneiss, and leucogranitic veins, as well as mantling metasediments. These samples were subjected to zircon U–Pb dating and monazite U–Pb dating, respectively. The analyses were conducted at the LA-ICP-MS laboratory at Nanjing University, following the protocol outlined by Jackson et al. (2004).

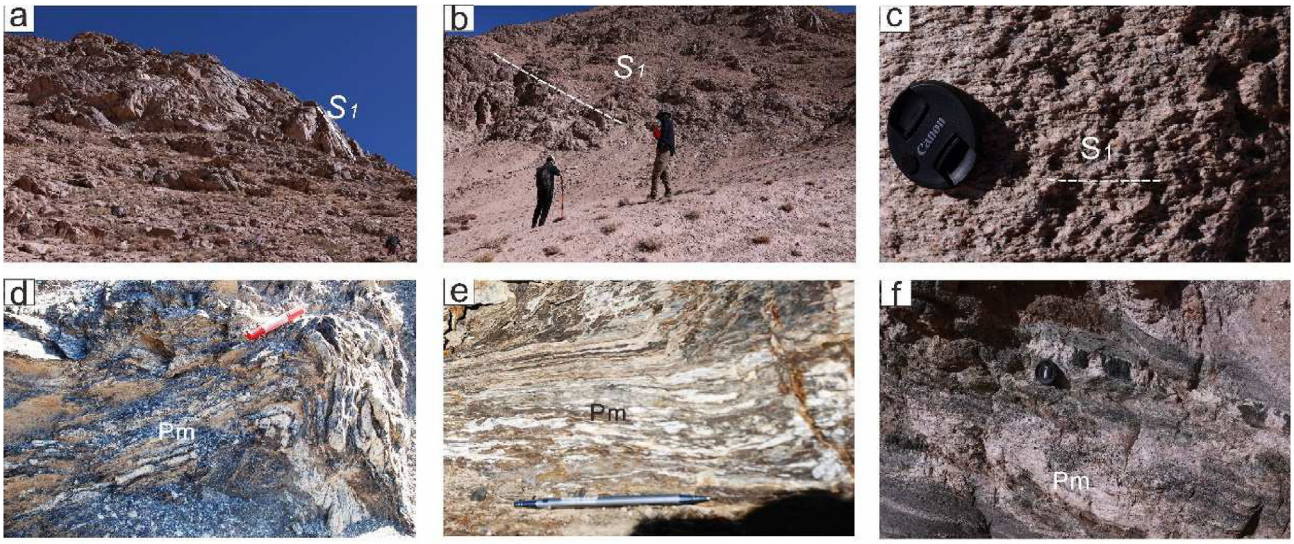

Fig. 11. Field photos from the Maeryang granitic gneiss and mantling Early Paleozoic-Triassic metasediments. The foliation (S1) of the granitic gneiss (a, b, c) and partial melting in the Early Paleozoic rocks (d, e, f) are shown.

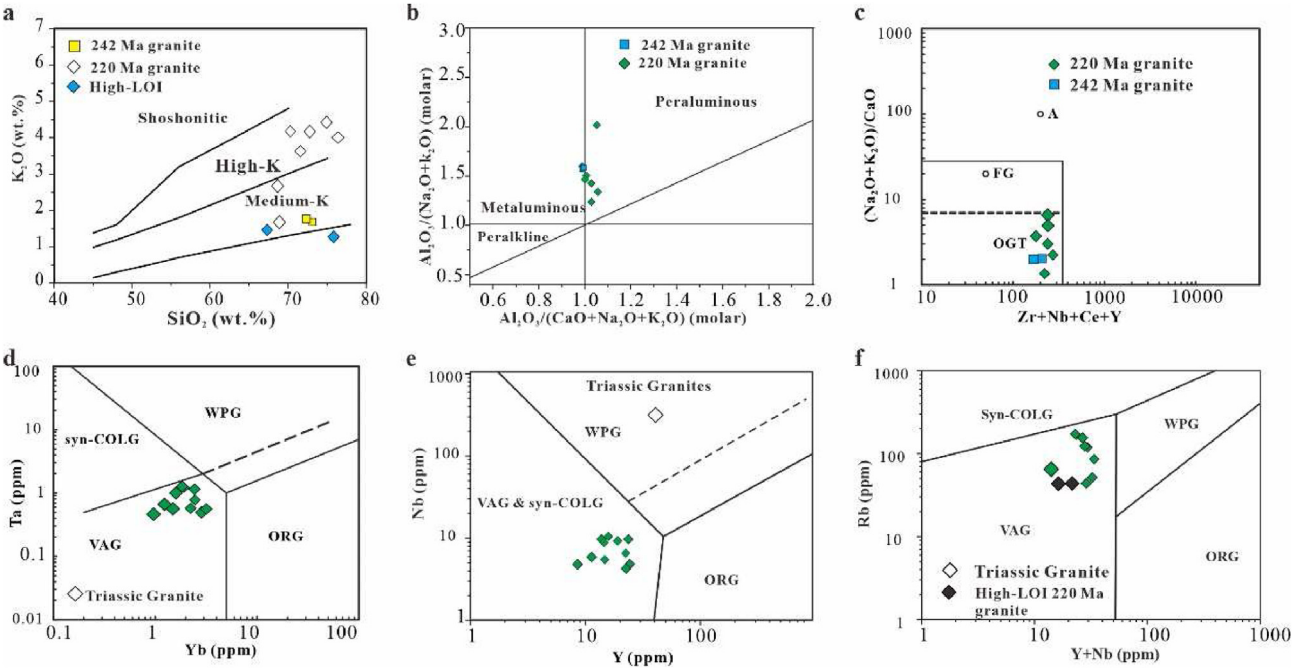

Fig. 12. Geochemical classification diagrams and tectonic discrimination diagrams for the Muztaghata granitic pluton. (a) SiO_2 vs. K_2O diagram (Peccerillo and Taylor, 1976); (b) ACNK vs. ANK diagram (Maniar and Piccoli, 1989); (c) Zr+Nb+Ce+Y vs. $(Na_2O+K_2O)/CaO$ diagram (Whalen et al., 1987); (d) Yb vs. Ta diagram (Pearce et al., 1984); (e) Nb vs. Y diagram (Pearce et al., 1984); (f) Rb vs. Y+Yb diagram (Pearce et al., 1984). WPG: within-plate granites; VAG: volcanic arc granites; Syn-COLG: syn-collision granites; Post-COLG: post-collision granites; ORG: oceanic ridge granites.

6.1. Zircon U–Pb dating for the Muztaghata gneiss dome

U–Pb dating of zircon has been carried out on a granodiorite sample P1-6(1) from the northern Muztaghata pluton intruding into the Carboniferous sequence, 10 samples from the KMGD including 3 granite samples P3-9(4), P3-10(6) and P5-4(1) from granites, 3 samples P4-1(4), R4-2(2) and P4-4(3) from granitic gneisses, 3 samples P6-13(1), P6-13(2) and P6-3(2) from the western Muztaghata migmatite and orthogneiss/granite intruding into the metamorphic rocks (Table S5). The zircon crystals selected showed good crystal morphology (euhedral to subhedral, prismatic shapes with aspect ratios of 1.2–2.5) and clear oscillatory zoning (Fig. S1), indicating a magmatic origin. Sample P1-6 (1) from the northern Kongur granitic pluton yields a weighted mean $^{206}Pb–^{238}U$ age of 243 ± 1 Ma (MSWD = 1.5, n = 14) (Fig. 14a). Samples P3-9(4), P3-10(6) and P5-4-1 from the granitic core yield weighted mean $^{206}Pb–^{238}U$ ages of 224 ± 2 Ma (MSWD = 1.7, n = 10),

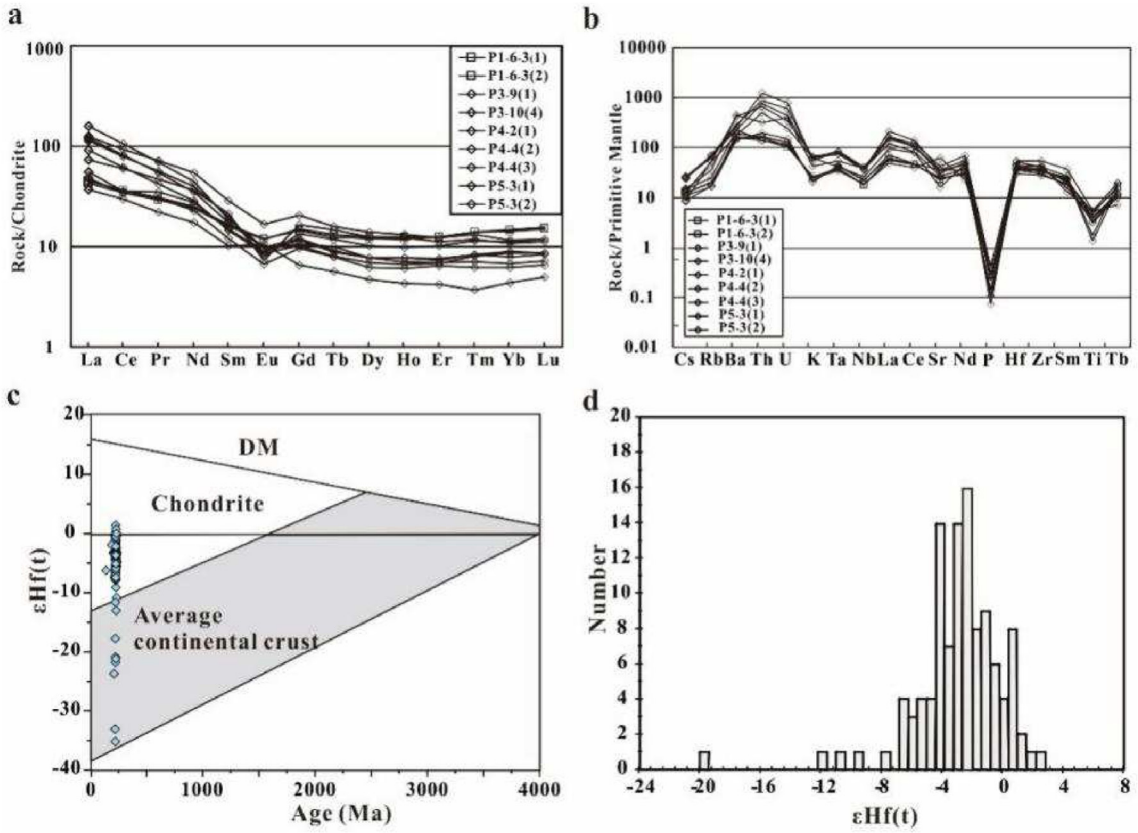

Fig. 13. (a–b) Chondrite-normalized REE patterns and primitive mantle-normalized trace elements spider diagrams. (c) εHf(t) vs. zircon U–Pb age plot, and (d) histograms of zircon εHf(t) value for the Muztaghata granitic pluton. The chondrite values were taken from Boynton (1984), and primitive mantle values from Sun and McDonough (1989).

217 ± 2 Ma (MSWD = 1.3, n = 23) and 220 ± 3 Ma (MSWD of 2.6, n = 15), respectively (Fig. 14 b-d). Samples P4-1(4), R4-2(2) and P4-4(3) from the Muztaghata granitic gneisses yield weighted mean ^{206}Pb–^{238}U ages of 212 ± 1 Ma, 211 ± 1 Ma, and 204 ± 1 Ma with MSWD of 2.2 (n = 12), 1.8 (n = 17) and 0.6 (n = 19), respectively (Fig. 14e–g). The magmatic zircons from samples P6-13(1), P6-13(2) and P6-3(2) have the weighted mean ^{206}Pb–^{238}U ages of 222 ± 3 (MSWD = 1.5, n = 15), 204 ± 1 Ma (MSWD = 0.8, n = 15), and 223 ± 2 Ma (MSWD = 1.9, n = 22), respectively (Fig. 14h–j).

Furthermore, we obtained a sample (P7-11(3)) from a syn-tectonic leucogranitic vein that intruded a mantling Sil-Ky-Gt-Bi schist in the Maeryang gneiss dome, and subjected it to zircon U–Pb dating analysis. The results showed a weighted mean age of 193.0 ± 1 Ma (MSWD = 0.9, n = 16, Fig. 14k), indicating a syntectono-thermal age for the Maeryang gneiss dome.

In addition, we conducted zircon U–Pb dating analyses on a garnet-bearing amphibolite (P5-2-14) and a metavolcanic rock (P5-2(15)) from the mantling metamorphic rocks on the eastern flank of the Muztaghata pluton. The samples yielded weighted mean ^{206}Pb–^{238}U ages of 444 ± 4 Ma (MSWD = 0.3, n = 13) and 436 ± 1 Ma (MSWD = 0.4, n = 14), respectively, indicating a Silurian protolith age (Fig. 14i-m).

6.2. Zircon U–Pb dating for the Maeryang pluton

Zircon U–Pb dating was conducted on three granitic gneiss samples (C2-5, C2-6 and C2-7) from the NW end of the Maeryang granitic gneiss zone. The LA-ICPMS method was used in Nanjing Hongchuang Exploration Technology Service Co., Ltd, with the Resolution SE model laser ablation system (Applied Spectra, USA) equipped with ATL (ATLEX 300) excimer laser and a Two Volume S155 ablation cell. The system was coupled to an Agilent 7900 ICPMS (Agilent, USA). The analytical method is described in detail in Jackson et al. (2004). The three samples have a mineral assemblage of biotite + feldspar + quartz ± muscovite, and most zircon crystals show euhedral to subhedral crystal morphology with core-mantle-rim structures. While most zircon mantles have clear oscillatory zoning indicating magmatic origin, most zircon cores do not. The rims of the zircons show clear signs of metasomatism, along with fractures and inclusions and evidence of partial metasomatism in the mantles and cores, suggesting a complicated history for these zircons.

The zircons with oscillatory zoning in their cores and mantles were dated in order to determine the time of magmatic petrogenesis and older events. To avoid complexity, rims, fractures, and inclusions were excluded from the analysis. The

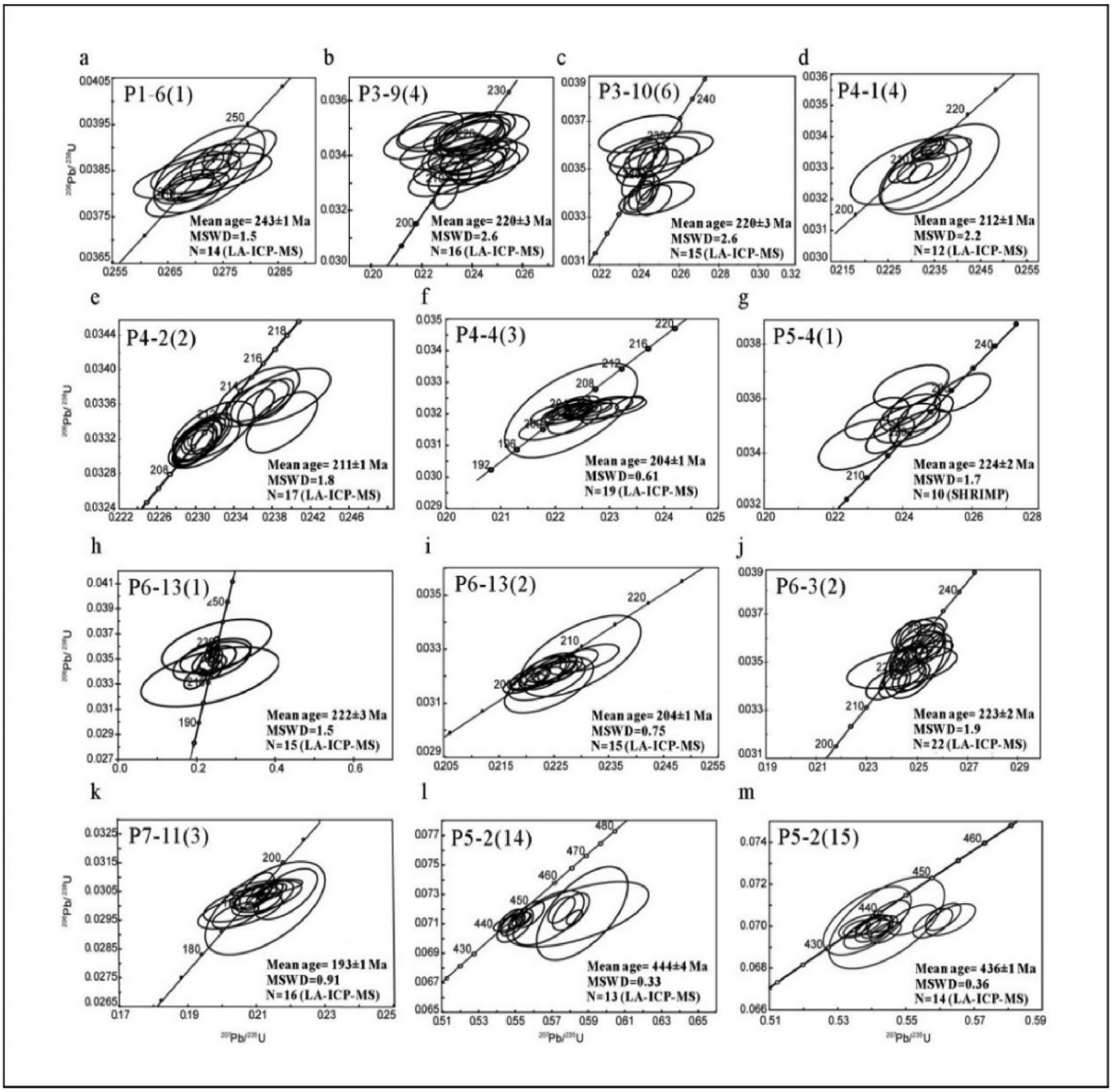

Fig. 14. Zircon U–Pb concordia diagrams for most samples from the Kongur granitic pluton (a), the Muztaghata pluton (b–j), and the eastern mélange zone (l–m). In addition, sample P7-11(3) (k) was collected from the mantling Triassic metasediments of the Maeryang gneiss dome. "Mean age" refers to "Mean ^{206}Pb–^{238}U age".

Th/U ratio of the dated zircons in these three samples ranges from 0.18 to 0.75, indicating a predominantly magmatic origin of the dated zircon zones. Sample C2-5 yielded a weighted mean ^{206}Pb–^{238}U age of 519 ± 2 Ma (MSWD = 0.2, n = 25). It also yielded two other older ^{206}Pb–^{238}U ages of 935 ± 14 Ma and 790 ± 9 Ma, which were probably dated in inherited zircon cores. Sample C2-6 yielded a weighted mean ^{206}Pb–^{238}U age of 517 ± 1 Ma (MSWD = 0.1, n = 28). Sample C2-7 yielded one ^{206}Pb–^{238}U age of 668 ± 9 Ma from an inherited zircon core. All other zircons in sample C2-7 revealed a weighted mean ^{206}Pb–^{238}U age of 514 ± 1 Ma (MSWD = 0.1, n = 32, Fig. 15). The results from these three samples are generally consistent.

6.3. In situ monazite U–Pb dating for the KMGD

Monazite, a mineral containing LREE, Th, and PO_4, can be used to determine ages of deformation and metamorphism (e.g., Parrish, 1990; Williams and Jercinovic, 2002; Dumond et al., 2008; Spear and Pyle, 2002, 2010; Spear, 2010; Foster et al., 2000; Foster and Parrish, 2003; Gibson et al., 2004). By investigating monazites from different structural positions, we can link absolute ages to specific chemical domains formed by metamorphic reactions and/or deformation events. To this end, we conducted an Electron Probe Micro Analysis (EPMA) using a Cameca SX100 Electron Microprobe, and we analyzed in-situ U–Th–Pb isotopes using a Laser Ablation Multi-

Collector Inductively Coupled Plasma Spectrometer system housed at the University of California, Santa Barbara. The analytical procedure is described in full detail in Cottle et al. (2009).

We collected sample P3-2 (29) from the SW end of the Kongur-Muztaghata gneiss dome and determined its mean weighted age to be 198 ± 1 Ma (MSWD = 4.1, n = 37, Table S7) using monazite dating. Zircon U–Pb dating of the same sample gave an age of ~21 Ma (Cai et al. 2017). This early Jurassic age is consistent with previous data from the west schist of the KMGD.

6.4. Monazite dating for the MYGD

Monazite grains embedded in the matrix of mylonitic metapelitic rocks were chosen from five samples of mylonitic garnet-sillimanite-biotite gneiss [P7-1(7), P7-3(1), P8-3(2), and P11-6(2)] in the MYGD, as well as one sample of garnet-biotite-plagioclase amphibolite [P8-2(11)] from the surrounding Triassic meta-sedimentary rocks. Microphotographs of monazite grains located along the foliation plane and in pressure shadows of garnet porphyroclasts from the mylonitic garnet-sillimanite-biotite gneiss [sample P7-1(7)], which formed during syntectonic deformation (Fig. S3).

Samples P7-1(7), P7-3(1), P8-2(11), P8-3(2), and P11-6(2) produced mean weighted ages of 197 ± 1 Ma (MSWD = 1.0, n = 18), 202 ± 2 Ma (MSWD = 2.3, n = 37), 202 ± 2 Ma (MSWD = 2.6, n = 25), 203 ± 2 Ma (MSWD = 7.5, n = 27), and 206 ± 2 Ma (MSWD = 3.6, n = 31), respectively (Table S7, Fig. 16). These results provide relevant ages for the metamorphic event of the mantling metamorphic rocks in the MYGD, which are approximately consistent with the deformation age of 197 Ma obtained from the zircon U–Pb dating of the syntectonic leucogranitic vein [sample P7-1(3)] from the MYGD. The data suggest that the deformation and metamorphism events of the MYGD primarily occurred during the Early Jurassic.

6.5. Biotite ^{40}Ar-^{39}Ar dating for the KMGD

Biotite ^{40}Ar-^{39}Ar dating was conducted on three samples collected from the Muztaghata granite in the KMGD. Sample P3-9(5), which is a granitic protomylonite from the core, yields a plateau age of 7.6 ± 0.1 Ma (MSWD = 1.7, Fig. 17a). Samples P4-4(1) and P4-6(13), which are mylonitic granitic gneisses, yield 5.9 ± 0.1 Ma (MSWD = 3.6, Figs. 17b) and 6.3 ± 0.2 Ma (MSWD = 2.6, Fig. 17c), respectively (Table S8).

7. Discussion

7.1. Affinity of the Kongur-Muztaghata-Maeryang terrane in the NE Pamir

The Kongur-Muztaghata pluton in the KMGD, which formed during the Triassic, exhibits calc-alkaline and metaaluminous or slightly peraluminous compositions, negative Nb, Ta and Ti anomalies, weakly fractionated REE patterns, and relatively low Y, Nb and Rb contents (Figs. 12 and 13). These features classify the pluton as a calc-alkaline I-type granitoid, a common component of subduction-related arc terranes. The northward subduction of the Paleo-Tethyan Jinsha oceanic slab is responsible for the formation of the arc terrane. Zircon grains from the Muztaghata pluton have fractionated REE patterns with LREE enrichment, HREE depletion, negative Eu anomalies, and essentially negative εHf(t) values, indicating the re-melting of ancient continental crustal materials (with TDM2 (Hf) model ages ranging from 2.5 to 1.1 Ga) and some minor input of juvenile components (possibly mantle origin) in the formation of the granites from which the zircons were collected (Fig. 13).

Typically, the crystallization of a large pluton within an arc terrane takes about 30 million years. Crystallization occurs first along the margin and later in the core of the pluton (e.g. Pupier et al., 2008). The granitic gneiss on the margin of the Kongur-Muztaghata granitic pluton has been dated at 254-227 Ma (Robinson et al., 2012; Imrecke et al., 2019), while the granitic core yields crystallization ages of ~224-210 Ma, as determined in this study.

The geochemical characteristics and crystalline ages of the Kongur-Muztaghata pluton are comparable to those of the Yidun pluton that formed between 245 and 216 Ma in the Songpan-Ganzi terrane, as indicated by previous studies (Reid et al., 2007; Gao et al., 2018). Similarly, the surrounding rocks of the KMGD are analogous to those of the Songpan-Ganzi

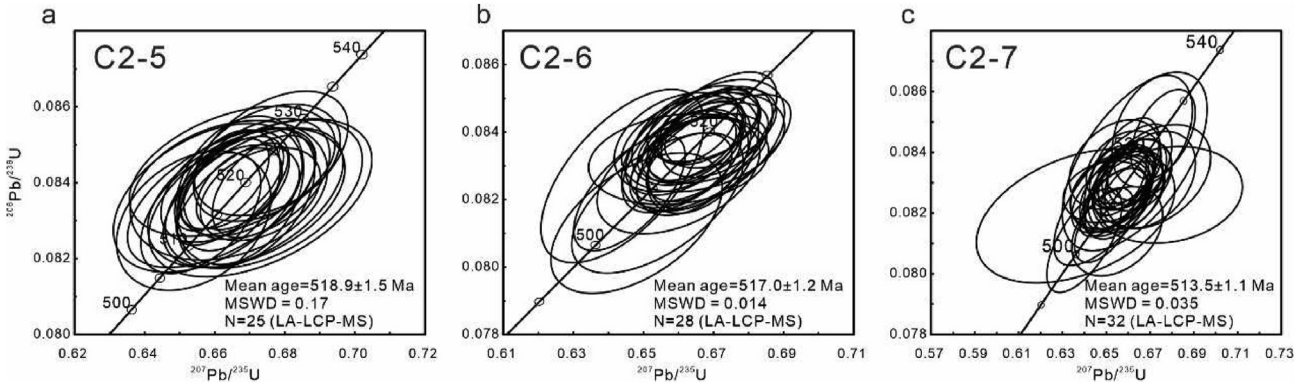

Fig. 15. Zircon U–Pb concordia diagrams for the samples from the Myeryang granitic gneiss. "Mean age" refers to "Mean ^{206}Pb–^{238}U age".

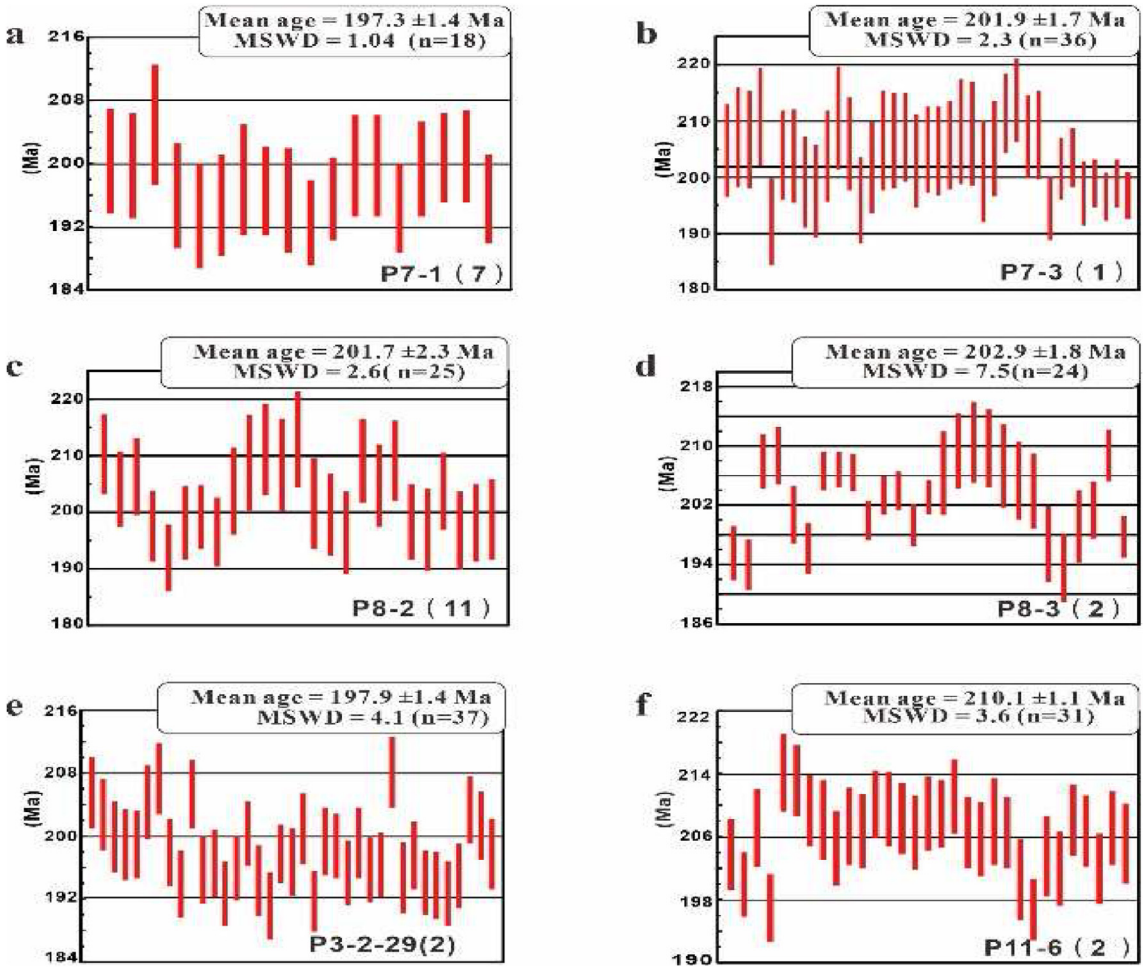

Fig. 16. Diagrams of monazite ages for samples P7-1(7), P7-3(1), P8-2(11), P8-3(2) and P11-6 (2) from the mantling metamorphic rocks of the MYGD. Sample P3-2(29) was collected along the WMSZ of the KMGD (Cai et al., 2017). "Mean age" refers to "Mean ^{206}Pb–^{238}U age".

terrane in the northern Tibet Plateau (Xu et al., 1992). This suggests that the geological origin and tectonic process of these two regions, which are geographically distant, were linked and synchronous.

In the southern KMGD, the Maeryang gneiss dome exhibits Cambrian granitic gneiss in the core and Early Paleozoic-Triassic sequence in the mantle. While the cores of Maeryang and Kongur-Muztaghata gneiss domes differ in their compositions and ages, they both experienced a Late Triassic-Early Jurassic thermo-tectonic event that was similar to that of the Songpan-Ganze terrane in the northern Tibetan Plateau. Thus, we propose that the Kongur-Muztaghata-Maeryang terrane in the NE Pamir represents the western extension of the Songpan-Ganze terrane in the northern Tibetan Plateau. In addition, our new data indicate for the first time that the granites and volcanic rocks in the core of the MYGD and KMGD formed during a Pan-African event.

7.2. Barrovian and Buchan metamorphisms in gneiss domes of the NE Pamir

Barrovian metamorphism refers to metamorphism that occurs under moderate geothermal gradients, as originally proposed by Barrow (1893, 1912). Barrow (1893) first proposed a sequence of Barrovian-style metamorphic minerals, progressing from lower to higher metamorphic grades: chlorite, biotite, garnet, staurolite, kyanite, and sillimanite. Barrovian metamorphism is typically associated with continental collision (England and Thompson, 1984) and is commonly observed in orogenic belts such as the Himalayan, Alpine, Qinling, and Appalachian orogenic belts (Berger et al., 2011; Gaidies et al., 2014; Jiang et al., 2015; Skrzypek et al., 2015). The traditional model suggests that Barrovian metamorphism is the result of the thermal relaxation process of thickened crust (England and Thompson, 1984). However, recent studies have shown that thermal convection of magma intrusions in the middle crust can also lead to Barrovian metamorphism (Vorhies and Ague, 2011; Viete et al., 2013).

Buchan metamorphism, on the other hand, represents high-temperature and low-pressure metamorphism. The sequence of metamorphic minerals progresses from low to high grades: chlorite, biotite, garnet, staurolite, andalusite, and sillimanite (Read, 1924; Read, 1952, Fig. 2). Buchan metamorphism occurs in the Hercynian orogen, the New England orogen in Australia, and other orogens affected by thermal events (Craven et al., 2012; Košuličová and Štípská,

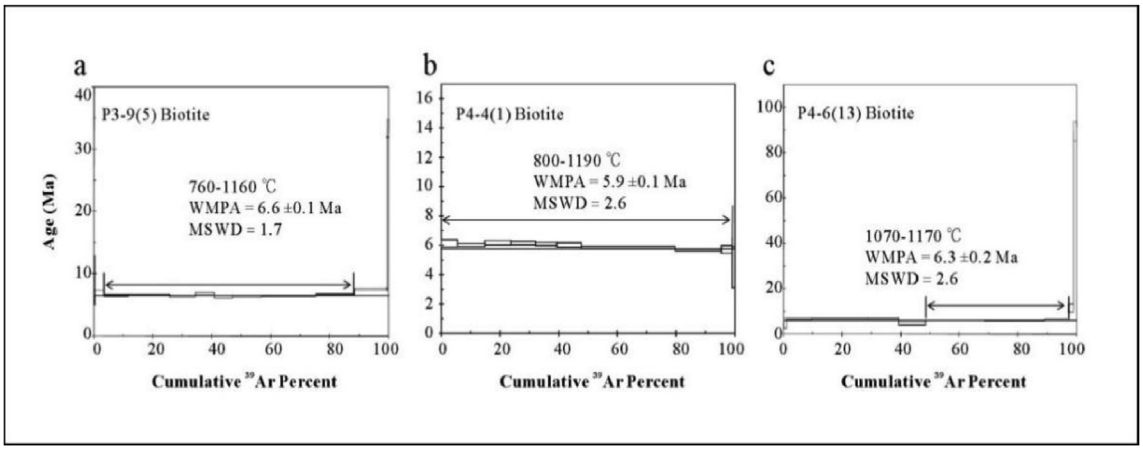

Fig. 17. Biotite ^{40}Ar/^{39}Ar plateau ages for samples P3-9(5) (a), P4-4(1) (b), and P4-6-(13) (c) from the Muztaghata pluton.

2010; St-Onge and Davis, 2018). The high geothermal gradient of Buchan metamorphism may be caused by thermal convection resulting from emplacement of mantle-derived or granitic magma, or rapid exhumation of the deep crust (Craven et al., 2012). In general, the mantling metamorphic sedimentary rocks in gneiss domes commonly develop Barrovian and Buchan metamorphic belts or the superimposition of two metamorphic facies. For instance, the Northern Himalayan gneiss domes and central-southern Pamir gneiss domes (Lee et al., 2004; Schmidt et al., 2011; Zhang et al., 2012).

The mantling metasediments of the Kongur-Muztaghata and Maeryang gneiss domes show evidence of both Barrovian metamorphism (represented by kyanite) and Buchan metamorphism (represented by andalusite). This suggests that the rocks underwent a superimposition of medium-pressure and high-temperature Barrovian metamorphism, followed by a Buchan-type high-temperature and lower-pressure metamorphism. We propose that the mantling meta-pelitic rocks initially experienced Barrovian metamorphism in the deep crust, followed by Buchan-type metamorphism that occurred synchronously with the initial uplift of the KMGD under decompression conditions. We suggest that the Barrovian and Buchan metamorphisms observed in the Kongur-Muztaghata and Maeryang gneiss domes of the NE Pamir are similar to those observed in the gneiss domes of the Songpan-Ganze terrane.

7.3. Genesis and initiation of KMGD and MYGD

Previous studies (Cai et al., 2017) have reported that the West Muztaghata Shear Zone (WMSZ) located on the western flank of the KMGD exhibits gentle west-dipping foliations, mylonitization, and top-to-the-west or southwest shear sense (Fig. 2). The authors suggest that the WMSZ formed at around 20 Ma ago, based on zircon U–Pb data from syntectonic felsic veins and mica ^{40}Ar-^{39}Ar data, and underwent continuous exhumation into the upper crust until 12-8 Ma. Previous researchers have proposed that the KMGD was partially accommodated by the Cenozoic south-north striking, west-dipping detachment during the period of 21-8 Ma (Robinson et al., 2004, 2007, 2010; Cai et al., 2017; Rutte et al., 2017a; Rutte et al., 2017b; Imrecke et al., 2019). The Cenozoic intense tectono-thermal event triggered by the collision between the Asian and Indian plates often obscures and obliterates pre-Cenozoic records. This is why we aim to investigate pre-Cenozoic records.

Our new geochronological results have led to a revision of the previous understanding of the Mustaghata pluton's western flank, as follows.

(1) The Monazite U–Pb dating from the West Muztaghata shear zone (WMSZ) previously dated at ~20 Ma by Cai et al. (2017) has been reevaluated and we obtained a new age of ~197 Ma from the mantling Early Paleozoic high-grade metamorphic rock.
(2) We have also identified new ages using in-situ monazite U–Pb data for samples P7-2, P7-3, P8-2, P8-3, and P11-6, which date back to ~206-189 Ma. Additionally, previous results from samples D051 and D052, which were dated using U–Pb data from Zircon metamorphic rim (Zhang et al., 2018), were found to be ~193–200 Ma. These new ages were identified in mantling Early Paleozoic-Triassic Barrovian-Buchan metamorphic rocks of the Maeryang gneiss dome. Furthermore, we discovered that a syntectonic laucogranitic vein (sample P7-2) in the mantle Triassic Sillimanite-bearing schist of the Maeryang gneiss dated back to ~197 Ma using zircon U–Pb data.

The new geochronological results presented above are in agreement with some previous data. For instance, Robinson et al. (2012) reported a Late Triassic depositional age of ~204 ± 2 Ma and Early Jurassic metamorphic event ages of 190–170 Ma for their sample AR6-22-00-1, which is an amphibolite-facies (garnet + sillimanite) quartz-rich schist collected from the western flanks of the MYGD (Fig. 2). Their detrital zircon analysis of sample AR8-31-03-1, an upper amphibolite-facies (kyanite + K-feldspar) quartz-rich schist,

yielded a Paleozoic depositional age of 459 ± 6 Ma and a peak metamorphic age of 190 Ma (Fig. 2).

Thus, the Late Triassic-Jurassic Buchan-type medial-temperature and lower-pressure metamorphism was synchronous with the initial uplift of the KMGD and MYGD. This thermos-tectonic event is a significant factor that cannot be ignored. The KMGD and MYGD serve as an example of how lithological, thermal, rheological, and kinematic factors have combined to control the initiation and development of the gneiss dome within a wide collisional orogenic zone.

7.4. Multi-stage evolution of the KMGD

The results of this study, combined with previously published data, enable us to propose a multi-stage evolution model of the KMGD since the Triassic period (Fig. 18).

(1) During the northward subduction of the Paleo-Tethys Jinsha oceanic slab and the subsequent collision of Kongur-Muztagnata arc with west Kunlun and Qiangtang terranes in the late Permian–Triassic, the re-melting of ancient continental crustal materials and plutonism formed the Kongur-Muztagnata pluton in the northern Pamir, under conditions of high-grade Barrovian-type metamorphism (Fig. 18a). The MT–MP Barrovian metamorphism occurred concurrently with orogenic compressional deformation, crustal thickness, and re-melting in the lower crust of the Kongur-Muztagnata arc terrane. Dome exhumation occurred from the deep to the middle crust under a syn-tectonic decompressional condition, constrained by in-situ monazite U–Pb dating and zircon U–Pb dating from syn-tectonic leucogranitic veins, at ~206-193 Ma (Fig. 18b).

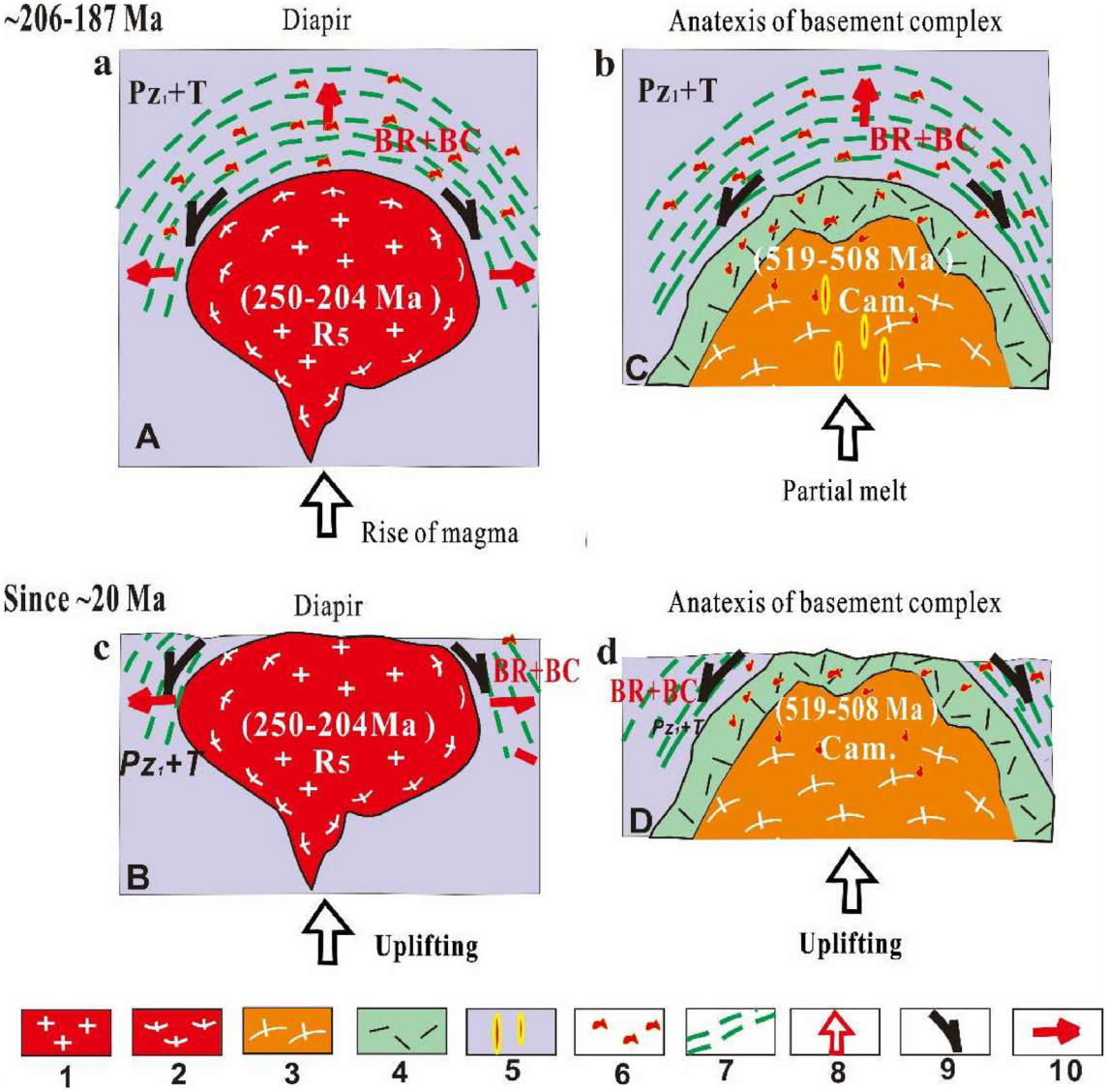

Fig. 18. Proposed tectonic model for the gneiss domes in the NE Pamir. (A) Diapir model of the Kongur-Muztaghata gneiss dome; (B) Anatexis basement complex model of the Maeryang gneiss dome. 1, Triassic granite; 2, Triassic granitic gneiss; 3, Cambrian granitic gneiss; 4, Cambrian volcanic rocks; 5, Partial melting flow; 6, Partial melting; 7, Metamorphic zone; 8, Rise of magma and partial melting; 9, Domal structure; 10, Strain directions. BR, Barrovian metamorphism; BC, Buchan metamorphism.

(2) The rapid exhumation of the KMGD from deep to shallow levels was a result of ongoing India–Asia continental collision and southward intracontinental subduction of the Tarim block beneath the North Pamir Terrane since the Miocene (Fig. 18b, d). The middle crustal materials with weak rheology accommodated tectonic extension effectively along the low-angle WKMD during the Oligocene-Miocene period (Stearns et al., 2013; Rutte et al., 2017a, Rutte et al., 2017b). The brittle normal faulting along the high-angle extensional system within the upper crust and removal of the upper crustal materials through tectonic denudation and erosion are the processes that resulted in cold, shallow exhumation. Thus, the KMGD provides insight into the autocatalytic relationship between detachment extension and diapirism in a hot, thick crust, which resulted from syntectonic decompressional partial melting and corresponds to the rapid dome exhumation from the deep to shallow crust. However, within the system of Miocene north-south extension, the Pre-Cenozoic structures were significantly overprinted by the late Cenozoic tectonism at ~20-8 Ma, as documented by zircon U–Pb and thermochronological data from the area (Robinson et al., 2012, 2015; Cai et al., 2017; and this study). Therefore, the KMGD recorded both the Late Triassic-Early Jurassic and Miocene events of tectonic deformation.

The Miocene extensional system is believed to include the West Kongur-Muztaghata normal Fault (WMSZ) to the west, the STF to the southwest, and the Ghez-Kuki (GF) steeply east-dipping normal ductile fault to the east (Arnaud et al., 1993; Brunel et al., 1994; Strecker et al., 1995; Robinson et al., 2004, 2007; Amidon and Hynek, 2010; Cao et al., 2013; Cai et al., 2017).

8. Conclusions

The Kongur-Muztaghata gneiss dome (KMGD) and the Maeryang gneiss dome (MYGD) are two distinct types of gneiss domes in the NE Pamir orogenic belt. The KMGD's core is composed of a Triassic granitoid pluton, while the MYGD's core is a pre-Ordovician complex. However, both consist of a common mantling Early Paleozoic to Triassic sequence that underwent HT-M/LP Barrovian-Buchan metamorphism during the Late Triassic-Jurassic period, indicating their initial uplift time. Our investigation reveals that the KMGD formed as magmatic diapirism, whereas the MYGD, as a gneiss dome of the anatexis complex, resulted from partial melting in the deep crust.

Therefore, the KMGD and the MYGD have undergone two main stages of exhumation. The first stage involved the initial domal exhumation from the deep crustduring the latest Triassic-Early Jurassic period (~206-193 Ma). This exhumation occurred during the closure of Paleo-Tethys oceanic and the collision of the Songpan-Ganze terrane with the west Kunlun and the Qiangtang terrane. The second stage involved the subsequent cold, shallow exhumation from the middle crust to the upper crust due to tectonic extension and denudation caused by brittle, high-angle normal faults since the Miocene. This study provides insight into how lithological, thermal, rheological, and kinematic factors have combined to control the initiation and development of gneiss domes within a wide, hot, thick collisional orogenic zone.

Declaration of competing interest

The authors declare that they have no known competing financial interests or personal relationships that could have appeared to influence the work reported in this paper.

Acknowledgments

This research received financial support from the National Natural Science Foundation of China (grants No. 91955203, No. 42272111, No. 40921001, and No. 42172263). The zircon U–Pb age was determined at the SHRIMP center in Beijing and the State Key Laboratory for Mineral Deposits Research at Nanjing University. Monazite U–Pb dating was carried out at the University of California, Santa Barbara, USA, and the ^{40}Ar-^{39}Ar dating was conducted at the Institute of Geology, Chinese Academy of Geological Sciences.

Appendix A. Supplementary data

Supplementary data to this article can be found online at https://doi.org/10.1016/j.sesci.2023.04.001.

References

Amidon, W.H., Hynek, S.A., 2010. Exhumational history of the north central Pamir. Tectonics 29, TC5017.

Arnaud, N.O., Brunel, M., Cantagrel, J.M., Tapponnier, P., 1993. High cooling and denudation rates at Kongur Shan, Eastern Pamir (Xinjiang, China) revealed by 40Ar/39Ar alkali feldspar thermochronology. Tectonics 12, 1335–1346.

Barrow, G., 1893. On an intrusion of muscovite-biotite gneiss in the south-eastern Highlands of Scotland, and its accompanying metamorphism. J. Geol. Soc. London 49 (1–4), 330–358.

Barrow, G., 1912. On the geology of lower Dee-side and the southern Highland Border. Proc. Geol. Assoc. 23 (5), 274–290.

Berger, A., Schmid, S.M., Engi, M., Bousquet, R., Wiederkehr, M., 2011. Mechanisms of mass and heat transport during Barrovian metamorphism: a discussion based on field evidence from the Central Alps (Switzerland/northern Italy). Tectonics 30 (1), 1–17.

Blichert-Toft, J., Albarède, F., 1999. Hf isotopic compositions of the Hawaii Scientific Drilling Project Core and the source mineralogy of Hawaiian basalts. Geophys. Res. Lett. 26, 935–938.

Bouilhol, P., Jagoutz, O., Hanchar, J.M., Dudas, F.O., 2013. Dating the India–Eurasia collision through arc magmatic records. Earth Planet Sci. Lett. 366, 163–175.

Boynton, W.V., 1984. Chapter 3–cosmochemistry of the rare earth elements: meteorite studies. Dev. Geochem. 2, 63–114.

Brunel, M., Arnaud, N., Tapponnier, P., Pan, Y., Wang, Y., 1994. Kongur Shan normal fault: type example of mountain building assisted by extension (Karakoram fault, eastern Pamir). Geology 22, 707–710.

Burchfiel, B.C., Chen, Z.L., Liu, Y.P., Royden, L.H., 1995. Tectonics of the Longmen Shan and adjacent regions, central China. Int. Geol. Rev. 37 (8), 661–735. https://doi.org/10.1080/00206819509465424.

Burtman, V.S., Molnar, P.H., 1993. Geological and Geophysical Evidence for Deep Subduction of Continental Crust beneath the Pamir. Geological Society of America. Special Paper 281.

Burtman, V.S., 2010. Tien Shan, Pamir, and Tibet: history and geodynamics of phanerozoic oceanic basins. Geotectonics 44, 388–404.

Cai, Z.H., Xu, Z.Q., Cao, H., Robinson, A.C., Li, G.W., Xu, X.Y., 2017. Miocene exhumation of northeast Pamir: deformation and geo/thermochronological evidence from western Muztaghata shear zone and Kuke ductile shear zone. J. Struct. Geol. 102, 130–146.

Cao, K., Wang, G.C., Beek, P.V.D., Bernet, M., Zhang, K.X., 2013. Cenozoic thermo-tectonic evolution of the northeastern Pamir revealed by zircon and apatite fission-track thermochronology. Tectonophysics 589, 17–32.

Cao, K., Wang, G.C., Bernet, M., Beek, P.V.D., Zhang, K.X., 2015. Exhumation history of the West Kunlun mountains, northwestern Tibet: evidence for a long-lived, rejuvenated orogen. Earth Planet Sci. Lett. 432, 391–403.

Cottle, J.M., Jessup, M.J., Newell, D.L., Horstwood, M.S.A., Noble, S.R., Parrish, R.R., Waters, D.J., Searle, M.P., 2009. Geochronology of granulitized eclogite from the Ama Drime Massif: implications for the tectonic evolution of the south Tibetan Himalaya. Tectonics 28, TC1002.

Coutand, I., Strecker, M.R., Arrowsmith, J.R., Hilley, G., Thiede, R.C., Korjenkov, A., Omuraliev, M., 2002. Late Cenozoic tectonic development of the intramontane Alai Valley, (Pamir-Tien Shan region, central Asia): an example of intracontinental deformation due to the Indo-Eurasia collision. Tectonics 21 (6), 3-1–3-19. https://doi.org/10.1029/2002TC001358.

Cowgill, E., 2010. Cenozoic right-slip faulting along the eastern margin of the Pamir Salient, northwestern China. GSA Bulletin 122 (1–2), 145–161. https://doi.org/10.1130/B26520.1.

Craven, S.J., Daczko, N.R., Halpin, J.A., 2012. Thermal gradient and timing of high-T–low-P metamorphism in the Wongwibinda metamorphic complex, southern new England orogen, Australia. J. Metamorph. Geol. 30 (1), 3–20.

Debon, F., Afzali, H., Le Fort, P., Sonet, J., 1986. Plutonic belts in Afghanistan: typology, age and geodynamic setting. Mémoires des Sciences de la Terre, Nancy 47, 129–153.

de Sigoyer, J., Vanderhaeghe, O., Duchêne, S., Billerot, A., 2014. Generation and emplacement of Triassic granitoids within the Songpan Ganze accretionary-orogenic wedge in a context of slab retreat accommodated by tear faulting, Eastern Tibetan Plateau, China. J. Asian Earth Sci. 88, 192–216. https://doi.org/10.1016/j.jseaes.2014.01.010.

Dumond, G., McLean, N., Williams, M.L., Jercinovic, M.J., Bowring, S.A., 2008. High-resolution dating of granite petrogenesis and deformation in a lower crustal shear zone: Athabasca granulite terrane, western Canadian Shield. Chem. Geol. 254, 175–196.

England, P.C., Thompson, A.B., 1984. Pressure—temperature—time paths of regional metamorphism I. Heat transfer during the evolution of regions of thickened continental crust. J. Petrol. 25 (4), 894–928.

Eskola, P.E., 1948. The problem of mantling gneiss domes. Quarterly J. Geol. Soc. 104 (1–4), 461. https://doi.org/10.1144/GSL.JGS.1948.104.01-04.21.

Foster, G., Kinny, P., Vance, D., Prince, C., Harris, N., 2000. The significance of monazite U–Th–Pb age data in metamorphic assemblages: a combined study of monazite and garnet chronometry. Earth Planet Sci. Lett. 181, 327–340.

Frost, C.D., Bell, J.M., Frost, B.R., Chamberlain, K.R., 2001. Crustal growth by magmatic underplating: isotopic evidence from the northern Sherman batholith. Geology 29, 515–518.

Foster, G., Parrish, R.R., 2003. Metamorphic Monazite and the Generation of P-T-T Paths, vol. 220. Geological Society London Special Publications, pp. 25–47.

Fu, X.F., Hou, L.W., Liang, B., 2017. Jiajika-type Granite-Pegmatite Lithium Deposit: Metallogenic Model and Three-Dimensional Prospecting Model. Science Press, Beijing (in Chinese).

Gaidies, F., Petley-Agan, A., Chakraborty, S., Dasgupta, S., Jones, P., 2014. Constraining the conditions of Barrovian metamorphism in Sikkim, India: P-T-t paths of garnet crystallization in the Lesser Himalayan Belt. J. Metamorph. Geol. 33 (1), 23–44.

Gao, X., Yang, L.Q., Orovan, E.A., 2018. The lithospheric architecture of two subterranes in the eastern Yidun Terrane, East Tethys: insights from Hf–Nd isotopic mapping. Gondwana Res. 62, 127–143.

Gibson, H.D., Carr, S.D., Brown, R.L., Hamilton, M.A., 2004. Correlations between chemical and age domains in monazite, and metamorphic reactions involving major pelitic phases: an integration of ID-TIMS and SHRIMP geochronology with Y–Th–U X-ray mapping. Chem. Geol. 211, 237–260.

Green, T.H., 1994. Experimental studies of trace-element partitioning applicable to igneous petrogenesis: sedona 16 years later. Chem. Geol. 117, 1–36.

Hacker, B.R., Ratschbacher, L., Rutte, D., Stearns, M., Malz, Stübner, K., Kylander-Clark, A.R., Pfander, J., Everson, A., 2017. Building the Pamir-Tibetan Plateau-Crustal stacking, extensional collapse, and lateral extrusion in the Pamir: 3. thermarometry and petrochronology of deep Asian crust. Tectonics 36, 1743–1766. https://doi.org/10.1002/2016TC00488.

Hsü, K.J., Guitang, P., Sengör, A.M.C., 1995. Tectonic evolution of the Tibetan plateau: a working hypothesis based on the Archipelago model of orogenesis. Int. Geol. Rev. 37 (6), 473–508. https://doi.org/10.1080/00206819509465414.

Hubbard, M.S., Grew, E., Hodges, K., Yates, M., 1997. Neogene cooling and exhumation in the southwest Pamir mountains, Tadjikistan. GSA Abstr. Prog. 29, 469.

Imrecke, D.B., Robinson, A.C., Owen, L.A., Chen, J., Schoenbohm, L.M., Hedrick, K.A., Lapen, T.J., Li, W.Q., Yuan, Z.D., 2019. Mesozoic evolution of the eastern Pamir. Lithosphere 11 (4), 560–580.

Jackson, S.E., Pearson, N.J., Griffin, W.L., Belousova, E.A., 2004. The application of laser ablation-inductively coupled plasma-mass spectrometry to in situ U-Pb zircon geochronology. Chem. Geol. 211, 47–69.

Jiang, Y.H., Jia, R.Y., Liu, Z., Liao, S.Y., Zhao, P., Zhou, Q., 2013. Origin of Middle Triassic high-K calc-alkaline granitoids and their potassic microgranular enclaves from the western Kunlun orogen, northwest China: a record of the closure of Paleo-Tethys. Lithos 156–159, 13–30. https://doi.org/10.1016/j.lithos.2012.10.004.

Jiang, Y.D., Štípská, P., Sun, M., Schulmann, K., Zhang, J., Wu, Q.H., Long, X.P., Yuan, C., Racek, M., Zhao, G.C., 2015. Juxtaposition of Barrovian and migmatite domains in the Chinese Altai: a result of crustal thickening followed by doming of partially molten lower crust. J. Metamorph. Geol. 33 (1), 45–70.

Košuličová, M., Štípská, P., 2010. Variations in the transient prograde geothermal gradient from chloritoid-staurolite equilibria: a case study from the Barrovian and Buchan-type domains in the Bohemian Massif. J. Metamorph. Geol. 25 (1), 19–36.

Lacassin, R., Valli, F., Arnaud, N., Leloup, P.H., Paquette, J.L., Li, H., Tapponnier, P., Chevalier, M.L., Guillot, S., Maheo, G., 2004. Large-scale geometry, offset and kinematic evolution of the Karakorum fault, Tibet. Earth Planet Sci. Lett. 219, 255–269.

Lee, J., Hacker, B., Yu, W., 2004. Evolution of North Himalayan gneiss domes: structural and metamorphic studies in Mabja Dome, southern Tibet. J. Struct. Geol. 26 (12), 2297–2316.

Liu, Z., Jiang, Y.H., Jia, R.Y., Zhao, P., Zhou, Q., 2015. Origin of Late Triassic high-K calc-alkaline granitoids and their potassic microgranular enclaves from the western Tibet Plateau, northwest China: implications for Paleo-Tethys evolution. Gondwana Res. 27 (1), 326–341. https://doi.org/10.1016/j.gr.2013.09.022.

Maniar, P.D., Piccoli, P.M., 1989. Tectonic discrimination of granitoids. Geol. Soc. Am. Bull. 101 (5), 635–643.

Mattauer, M., Malavielle, J., Calassou, S., Lancelot, J., Roger, F., Hao, Z., Xu, Z., Hou, L., 1992. La chaine triasique de Songpan-Ganze (oust Sichun at est Tibet): une chaine de plissment-decollement sur marge passive. Comptes rendus de L'Academie des Sciences Paris 6 (314), 619–626.

Parrish, R.R., 1990. U-Pb dating of monazite and its application to geological problems. Can. J. Earth Sci. 27, 1431–1450.

Pearce, J.A., Harris, N.B.W., Tindle, A.G., 1984. Trace element discrimination diagrams for the tectonic interpretation of granitic rocks. J. Petrol. 25, 956–983.

Peccerillo, A., Taylor, S.R., 1976. Geochemistry of Eocene calc-alkaline volcanic rocks from the Kastamonu area, Northern Turkey. Contrib. Mineral. Petrol. 58, 63–81.

Pupier, E., Barbey, P., Toplis, M.J., Bussy, F., 2008. Igneous layering, fractional crystallization and growth of granitic plutons: the Dolbel batholith in SW Niger. J. Petrol. 49 (6), 1043–1068. https://doi.org/10.1093/petrology/egn017.

Ratschbacher, L., Schwab, M., Semiletkin, S., Hacker, B., Hermann, U., 1997. The NE-edge of Tibet: intracontinental shortening and extension, basement doming, and exhumation in the Pamirs. GSA Abstr. Prog. 26, 144.

Reid, A.J., Fowler, A.P., Phillips, D., Wilson, C.J.L., 2005a. Thermochronology of the Yidun Arc, central eastern Tibetan Plateau: constraints from 40Ar/39Ar K-feldspar and apatite fission track data. J. Asian Earth Sci. 25 (6), 915–935. https://doi.org/10.1016/j.jseaes.2004.09.002.

Reid, A.J., Wilson, C.J.L., Phillips, D., Liu, S., 2005b. Mesozoic cooling across the Yidun Arc, central-eastern Tibetan Plateau: a reconnaissance 40Ar/39Ar study. Tectonophysics 398 (1–2), 45–66. https://doi.org/10.1016/j.tecto.2005.01.002.

Reid, A., Wilson, C.J.L., Shun, L., Pearson, N., 2007. Mesozoic plutons of the Yidun Arc, SW China: U/Pb geochronology and Hf isotopic signature. Ore Geol. Rev. 31 (1–4), 88–106.

Robinson, A.C., Yin, A., Manning, C.E., Harrison, T.M., Zhang, S.H., Wang, X.F., 2004. Tectonic evolution of the northeastern Pamir: constraints from the northern portion of the Cenozoic Kongur Shan extensional system, western China. Geol. Soc. Am. Bull. 116, 953.

Robinson, A.C., Yin, A., Manning, C.E., Harrison, T.M., Zhang, S.H., Wang, X.F., 2007. Cenozoic evolution of the eastern Pamir: implications for strain-accommodation mechanisms at the western end of the Himalayan-Tibetan orogen. Geol. Soc. Am. Bull. 119, 882–896.

Robinson, A.C., 2009. Geologic offsets across the northern Karakorum fault: implications for its role and terrane correlations in the western Himalayan-Tibetan orogen. Earth Planet Sci. Lett. 279, 123–130.

Robinson, A.C., Yin, A., Lovera, O.M., 2010. The role of footwall deformation and denudation in controlling cooling age patterns of detachment systems: an application to the Kongur Shan extensional system in the Eastern Pamir, China. Tectonophysics 496, 28–43.

Robinson, A.C., Ducea, M., Lapen, T.J., 2012. Detrital zircon and isotopic constraints on the crustal architecture and tectonic evolution of the northeastern Pamir. Tectonics 31, TC2016.

Robinson, A.C., 2015. Mesozoic tectonics of the Gondwanan terranes of the Pamir plateau. J. Asian Earth Sci. 102, 170–179.

Read, H.H., 1924. The geology of the country round Banff, Huntly and Turriff. J. Geol. 32, 86–96.

Read, H.H., 1952. Metamorphism and migmatisation in the Ythan valley, Aberdeenshire. Trans. Edinb. Geol. Soc. 15, 256–279.

Roger, F., Jolivet, M., Malavieille, J., 2010. The tectonic evolution of the Songpan-Garzê (North Tibet) and adjacent areas from Proterozoic to Present: a synthesis. J. Asian Earth Sci. 39 (4), 254–269. https://doi.org/10.1016/j.jseaes.2010.03.008.

Rumelhart, P.E., An, Y., 1999. Cenozoic vertical-axis rotation of the Altyn Tagh fault system. Geology 27, 480.

Rutte, D., Ratschbacher, L., Schneider, S., Stübner, K., Stearns, M.A., Gulzar, M.A., Hacker, B.R., 2017a. Building the Pamir-Tibetan Plateau-Crustal stacking, extensional collapse, and lateral extrusion in the Central Pamir: 1. Geometry and kinematics. Tectonics 36 (3), 342–384. https://doi.org/10.1002/2016TC004293.

Rutte, D., Ratschbacher, L., Khan, J., Stübner, K., Hacker, B.R., Stearns, M.A., Enkelmann, E., Jonckheere, R., Pfänder, J.A., Sperner, B., Tichomirowa, M., 2017b. Building the Pamir-Tibetan Plateau-Crustal stacking, extensional collapse, and lateral extrusion in the Central Pamir: 2. Timing and rates. Tectonics 36 (3), 385–419. https://doi.org/10.1002/2016TC004294.

Scherer, E., Münker, C., Mezger, K., 2001. Calibration of the lutetium-hafnium clock. Science 293, 683–687.

Schmidt, J., Hacker, B.R., Ratschbacher, L., Stübner, K., Stearns, M., Kylander-Clark, A., Cottle, J.M., Alexander, A., Webb, G., Gehrels, G., 2011a. Cenozoic deep crust in the Pamir. Earth Planet Sci. Lett. 312, 411–421.

Schneider, D.A., Edwards, M.A., Kidd, W.S.F., Khan, M.A., Seeber, L., Zeitler, P.K., 1999. Tectonics of Nanga Parbat, western Himalaya: synkinematic plutonism within the doubly vergent shear zones of a crustal-scale pop-up structure. Geology 27, 999–1002.

Schwab, M., Ratschbacher, L., Siebel, W., Mcwilliams, M., Minaev, V., Lutkov, V., Chen, F., Stanek, K., Nelson, B., Frisch, W., 2004. Assembly of the Pamirs: age and origin of magmatic belts from the southern Tien Shan to the southern Pamirs and their relation to Tibet. Tectonics 23, TC4002.

Sengör, A., Hsü, K., 1984. The Cimmerides of eastern Asia: history of the eastern end of Paleo-Tethys. Mem. Soc. Geol. France 147, 139–167.

Şengör, A.M.C., Natal'in, B.A., Burtman, V.S., 1993. Evolution of the Altaid tectonic collage and Paleozoic crustal growth in Eurasia. Nature 364, 299–307.

Skrzypek, E., Lehmann, J., Szczepański, J., Anczkiewicz, R., Štípská, P., Schulmann, K., Kröner, A., Białek, D., 2015. Time-scale of deformation and intertectonic phases revealed by P-T-D-t relationships in the orogenic middle crust of the Orlica-Śnieżnik Dome, Polish/Czech Central Sudetes. J. Metamorph. Geol. 32 (9), 981–1003.

Sobel, E.R., Dumitru, T.A., 1997. Thrusting and exhumation around the margins of the western Tarim basin during the India-Asia collision. J. Geophys. Res. Solid Earth 102, 5043–5063.

Sobel, E.R., Schoenbohm, L.M., Chen, J., Thiede, R., Stockli, D.F., Sudo, M., Strecker, M.R., 2011. Late Miocene-pliocene deceleration of dextral slip between Pamir and Tarim: implications for Pamir orogenesis: earth planet. Sci. Lett. 304 (3–4), 369–378.

Spear, F.S., Pyle, J.M., 2002. Apatite, monazite, and xenotime in metamorphic rocks. Rev. Mineral. Geochem. 48, 293–335.

Spear, F.S., 2010. Monazite–allanite phase relations in metapelites. Chem. Geol. 279, 55–62.

Spear, F.S., Pyle, J.M., 2010. Theoretical modeling of monazite growth in a low-Ca metapelite. Chem. Geol. 273, 111–119.

Strecker, M.R., Frisch, W., Hamburger, M.W., Ratschbacher, L., Semiletkin, S., Zamoruyev, A., Sturchio, N., 1995. Quaternary deformation in the eastern pamirs, Tadzhikistan and Kyrgyzstan. Tectonics 14, 1061–1079.

Stearns, M.A., Hacker, B.R., Ratschbacher, L., Lee, J., Cottle, J.M., Kylander-Clark, A., 2013. Synchronous Oligocene–Miocene metamorphism of the Pamir and the north Himalaya driven by plate-scale dynamics. Geology 41 (10), 1071–1074.

St-Onge, M.R., Davis, W.J., 2018. Wopmay orogen revisited: phase equilibria modeling, detrital zircon geochronology, and U-Pb monazite dating of a regional Buchan-type metamorphic sequence. Geol. Soc. Am. Bull. 130 (3–4), 678–704.

Stübner, K., Ratschbacher, L., Rutte, D., Stanek, K., Minaev, V., Wiesinger, M., Gloaguen, R., 2013. The giant Shakhdara migmatitic gneiss dome, Pamir, India-Asia collision zone: 1. Geometry and kinematics. Tectonics 32, 948–979. https://doi.org/10.1002/tect.20057.

Sun, S.S., Mcdonough, W.F., 1989. Chemical and isotopic systematics of oceanic basalts: implications for mantle composition and processes. Geol. Soc. London Spl. Pub. 42, 313–345.

Tapponnier, P., Mattauer, M., Proust, F., Cassaigneau, C., 1981. Mesozoic ophiolites, sutures, and large-scale tectonic movements in Afghanistan. Earth Planet Sci. Lett. 52, 355–371.

Taylor, S.R., McLennan, S.M., 1985. The Continental Crust: its Composition and Evolution. Blackwell Scientific Publications, United States.

Teyssier, C., Whitney, D.L., 2002. Gneiss domes and orogeny. Geology 30 (12), 1139. https://doi.org/10.1130/0091-7613(2002)030<1139:GDAO>2.0.CO;2.

Thiede, R.C., Sobel, E.R., Chen, J., Schoenbohm, L.M., Stockli, D.F., Sudo, M., Strecker, M.R., 2013. Late Cenozoic extension and crustal doming in the India-Eurasia collision zone: new thermochronologic constraints from the NE Chinese Pamir. Tectonics 32 (3), 763–779.

Thomas, J.C., Chauvin, A., Gapais, D., Bazhenov, M.L., Perroud, H., Cobbold, P.R., Burtman, V.S., 1994. Paleomagnetic evidence for Cenozoic block rotations in the Tadjik depression (central Asia). J. Geophys. Res. Solid Earth 99, 15141–15160.

Valli, F., Leloup, P., Paquette, J., Arnaud, N., Li, H., Tapponnier, P., Lacassin, R., Guillot, S., Liu, D., Deloule, E., Xu, Z., Mahéo, G., 2008. New U-Th/Pb constraints on timing of shearing and long-term slip-rate on the Karakoram fault. Tectonics 27, TC5007. https://doi.org/10.1029/2007TC002184.

Viete, D.R., Oliver, G., Fraser, G.L., Forster, M.A., Lister, G.S., 2013. Timing and heat sources for the Barrovian metamorphism. Scotland. Lithos 177, 148–163.

Vorhies, S.H., Ague, J.J., 2011. Pressure–temperature evolution and thermal regimes in the Barrovian zones, Scotland. J. Geol. Soc. London. 168 (5), 1147–1166. https://doi.org/10.1144/0016-76492010-073.

Weislogel, A.L., 2008. Tectonostratigraphic and geochronologic constraints on evolution of the northeast Paleotethys from the Songpan-Ganzi complex, central China. Tectonophysics 451 (1–4), 331–345. https://doi.org/10.1016/j.tecto.2007.11.053.

Whalen, J.B., Currie, K.L., Chappell, B.W., 1987. A-type granites: geochemical characteristics, discrimination and petrogenesis. Contrib. Mineral. Petrol. 95, 407–419.

Whitney, D.L., Teyssier, C., Vanderhaeghe, O., 2004. Gneiss domes and crustal flow. Spec. Pap. Geol. Soc. Am. 380, 15–33. https://doi.org/10.1130/0-8137-2380-9.15.

Williams, M.L., Jercinovic, M.J., 2002. Microprobe monazite geochronology: putting absolute time into microstructural analysis. J. Struct. Geol. 24, 1013–1028.

XBGMR (Xinjiang Bureau of Geology and Mineral Resources), 1993. Regional Geology of Xinjiang Uygur Autonomous Region. Geological Publishing House, Beijing (in Chinese with English abstract).

Xiao, W., Windley, B., Hao, J., Li, J., 2002. Arc-ophiolite obduction in the western Kunlun range (China): implications for the paleozoic evolution of central Asia. J. Geol. Soc. London 159 (5), 517–528. https://doi.org/10.1144/0016-764901-093.

Xiao, L., Zhang, H.F., Clemens, J.D., Wang, Q.W., Kan, Z.Z., Wang, K.M., Ni, P.Z., Liu, X.M., 2007. Late Triassic granitoids of the eastern margin of the Tibetan Plateau: geochronology, petrogenesis and implications for tectonic evolution. Lithos 96 (3–4), 436–452. https://doi.org/10.1016/j.lithos.2006.11.011.

Xu, Z.Q., Fu, X.F., Wang, R.C., Li, G.W., Zheng, Y.L., Zhao, Z.B., Lian, D.Y., 2020. Generation of lithium-bearing pegmatite deposits within the Songpan-Ganze orogenic belt, East Tibet. Lithos 354–355, 105281. https://doi.org/10.1016/j.lithos.2019.105281.

Xu, Z.Q., Hou, L.W., Wang, Z.X., 1992. Orogenic Process of Songpan-Ganze Orogenic Belt of China. Geological publishing House, Beijing (In Chinese).

Xu, Z.Q., Fu, X.F., Ma, X.X., Qi, X.X., Wu, C., Hou, L.W., Zhao, Z.B., 2016. The gneiss domes in Tibetan Plateau and their potential for prospecting. Acta Geol. Sin. 90 (11), 2971–2981. https://doi.org/10.3969/j.issn.0001-5717.2016.11.001 (in Chinese with English abstract).

Yang, W.Q., Liang, L., Cao, Y.T., Chao, W., He, S.P., Li, R.S., Zhu, X.H., 2010. Geochronological evidence of Indosinian (high-pressure) metamorphic event and its tectonic significance in Taxkorgan area of the Western Kunlun Mountains, NW China. Sci. China Earth Sci. 53, 1445–1459.

Yin, A., Harrison, T.M., 2000. Geologic evolution of the Himalayan-Tibetan orogen. Annu. Rev. Earth Planet Sci. 28 (1), 211–280.

Yin, A., Rumelhart, P.E., Butler, R., Cowgill, E., Harrison, T.M., Foster, D.A., Ingersoll, R.V., Zhang, Q.Q., Zhou, X.Q., Wang, X.F., 2002. Tectonic history of the Altyn Tagh fault system in northern Tibet inferred from Cenozoic sedimentation. Geol. Soc. Am. Bull. 114, 1257–1295.

Yin, A., 2004. Gneiss domes and gneiss dome systems. GSA (Geol. Soc. Am.) Spec. Pap. (Reg. Stud.) 380, 1–14.

Yuan, C., Zhou, M.F., Sun, M., Zhao, Y.J., Wilde, S., Long, X.P., Yan, D.P., 2010. Triassic granitoids in the eastern Songpan Ganzi Fold Belt, SW China: magmatic response to geodynamics of the deep lithosphere. Earth Planet Sci. Lett. 290 (3–4), 481–492. https://doi.org/10.1016/j.epsl.2010.01.005.

Zhang, C.L., Yu, H.M., Wang, A.G., Guo, K.Y., 2005. Dating of triassic granites in the West Kunlun mountains and its tectonic significance. Acta Geol. Sin. 79, 645–652 (in Chinese with English abstract).

Zhang, H.F., Zhang, L.F., Harris, N., Jin, L.L., Yuan, H.L., 2006. U–Pb zircon ages, geochemical and isotopic compositions of granitoids in Songpan-Garze fold belt, eastern Tibetan Plateau: constraints on petrogenesis and tectonic evolution of the basement. Contrib. Mineral. Petrol. 152 (1), 75–88. https://doi.org/10.1007/s00410-006-0095-2.

Zhang, H.F., Parrish, R., Zhang, L.F., Xu, W.C., Yuan, H.L., Gao, S., Crowley, Q.G., 2007. A-type granite and adakitic magmatism association in Songpan–Garze fold belt, eastern Tibetan Plateau: implication for lithospheric delamination. Lithos 97 (3–4), 323–335. https://doi.org/10.1016/j.lithos.2007.01.002.

Zhang, J., Santosh, M., Wang, X., Guo, L., Yang, X., Zhang, B., 2012. Tectonics of the northern Himalaya since the India–Asia collision. Gondwana Res. 21 (4), 939–960. https://doi.org/10.1016/j.gr.2011.11.004.

Zhang, Y., Niu, Y.L., Hu, Y., Liu, J.J., Ye, L., Kong, J.J., Duan, M., 2016. The syncollisional granitoid magmatism and continental crust growth in the West Kunlun Orogen, China – evidence from geochronology and geochemistry of the Arkarz pluton. Lithos 245, 191–204. https://doi.org/10.1016/j.lithos.2015.05.007.

Zhang, C.L., Zou, H.B., Ye, X.T., Chen, X.Y., 2018. Tectonic evolution of the NE section of the Pamir Plateau: new evidence from field observations and zircon U-Pb geochronology. Tectonophysics 723, 27–40.

Zhao, Z.B., Du, J.X., Liang, F.H., Wu, C., Liu, X.J., 2019. Structure and metamorphism of Markam gneiss dome from the eastern Tibetan Plateau and its implications for crustal thickening, metamorphism, and exhumation. G-cubed 20 (1), 24–45. https://doi.org/10.1029/2018GC007617.

Zheng, Y.L., Xu, Z.Q., Li, G.W., Lian, D.Y., Zhao, Z.B., Ma, Z.L., Gao, W.Q., 2020. Genesis of the Markam gneiss dome within the Songpan-Ganzi orogenic belt, eastern Tibetan Plateau. Lithos 362–363, 105475. https://doi.org/10.1016/j.lithos.2020.105475.